Astron. Astrophys. 226, 23–44 (1989)

ASTRONOMY AND ASTROPHYSICS

The stellar-free emission component in galactic nuclei: at low-levels, evidence for shock ionization*

C. Bonatto[1], E. Bica[1], and D. Alloin[2]

[1] Instituto de Fisica, UFRGS, C.P. 15051 Av. Bento Gonçalves 9500, Porto Alegre, RS, 91500, Brazil
[2] Observatoire de Paris, Département d'Astrophysique Extragalactique et de Cosmologie, F-92195 Meudon Cédex, France

Received August 9, 1988; accepted March 20, 1989

Summary. We have isolated the emission-line component in a sample of 92 galaxies using stellar absorption templates built from emission-free star cluster spectra. All sources of reddening extrinsic to the line emitting regions have been properly taken into account. A statistical analysis of the emission line properties has been carried out. We conclude, in particular, that the [N II] $\lambda\lambda$ 6548, 84 lines are slightly more sensitive to metallicity effects than the [S II] $\lambda\lambda$ 6717, 31 lines. However, both [N II] and [S II] lines are as well dependent on the excitation mechanism. The intrinsic reddening inferred from the Balmer emission line ratios is rather homogeneous as the Hα/Hβ line intensity ratio is peaked around the value 4.2. This indicates a remarkably uniform dust content in those regions building up the emission spectrum for a wide variety of objects: LINERS, nuclear H II regions, normal H II regions, Seyfert 2 nuclei and the narrow line region in Seyfert 1 nuclei.

From a subsample of 76 galaxies we have built three characteristic average spectra corresponding to (i) nuclear H II regions, (ii) objects identified as LINERS and (iii) extreme low-level emission galaxies with $W_{em}(H\alpha) \leq 2$ Å. For the latter class of objects we have been able to push down line measurements to an unprecedent level. We conclude from the [S II] $\lambda\lambda$ 6717, 6731/[S III] $\lambda\lambda$ 9069, 9532 line ratio that shock ionization is the mechanism at work in extreme low-level emission galaxies.

Key words: galaxies: active – nuclei – stellar content – interstellar medium: abundances – lines: formation

1. Introduction

The emission component in normal galaxy nuclei is dominated by forbidden lines from neutral or singly-ionized species which have been previously analyzed by e.g. Heckman (1980a,b), Stauffer (1982a,b) and Keel (1983). The emission component is in general severely entangled with the underlying stellar population. Thus it is extremely important to have *suitable stellar population templates* in order to isolate the emission component from nuclei within galaxies of various morphological types. Often, galaxy nuclei with an *almost* pure absorption component are employed as templates. However there always remains the doubt of a residual emission contribution, especially at Hα, in the template, even when this line is seen primarily in absorption. Furthermore it is practically impossible to find a blue galaxy nuclear population template without emission lines. A better approach to disentangle the emission contribution from the underlying stellar population is to use *model population templates*. Along this line Keel (1983) has employed population templates built from stellar spectra: these however were not of a metallicity large enough for representing massive galaxy nuclei.

Recently a method for population synthesis using a library of integrated spectra of star clusters has been developed (Bica, 1988 and references therein). This method is a two parameter analysis, age and metallicity. The initial mass function (IMF) and stellar evolution characteristics are implicit, as we use observed star cluster spectra. Thus it has been possible to derive suitable stellar population templates which are used in the present paper to obtain the pure emission component. The analysis of the *pure emission component* gives in galaxy nuclei an insight into the ionization mechanism at work in galaxy nuclei: does this mechanism differ according to the emission level? Two observational approaches can be used to answer this question. First, an analysis of individual galaxy spectra. In this case however, it is still very difficult to access lines like [O III] λ 5007 and [S III] λ 9532 in weak LINERS (Keel, 1983; Diaz, Pagel and Wilson, 1985, hereafter DPW), in spite of large progress achieved in detectors over the last decade. The near infrared region is moreover entangled with earth's atmosphere molecular bands. A second approach is to group objects and sum their spectra, according to similar properties, such as the intensity of strong emission lines. Thus, a higher signal to noise ratio can be achieved and in water-vapor contaminated regions, residues of these corrections are averaged out. It becomes then possible to measure emission lines to an unprecedently low-level: this in turn may clarify what is the dominant ionization source in the corresponding objects.

This paper develops as follows: in Sec. 2 we briefly present the observational data set and the galaxy sample; in Sect. 3 we give a few comments on the stellar population templates and their subtraction; in Sec. 4 we provide measurements of pure emission spectra and make comparisons with earlier works; in Sec. 5 we study the physical properties of the gas for the whole galaxy sample; in Sec. 6 we group objects in three classes for improvement of the data signal to noise ratio and hence for access to weak lines. This in turn provides information about the

Send offprint requests to: D. Alloin

* Based upon observations collected at the European Southern Observatory (La Silla)

ionization mechanism at work in each class of objects. Finally, we present in Sect. 7 some concluding remarks.

2. Observational data set and galaxy sample

The observational material was collected at ESO and consists of visible IDS spectra (Bica and Alloin, 1986a, hereafter BA 86a, a notation to be used all throughout for this series of papers; BA 87a) and near infrared CCD spectra (BA 87b). The spectral resolution is of the order of 10–12 Å. The original sample was made of 167 objects with IDS visible spectra. In the present analysis we have excluded 71 objects because of an absence or an only marginal evidence of emission. Galaxies NGC 1387, NGC 1398, NGC 4552, and NGC 7184 although showing weak emission lines were disregarded as well owing to low S/N ratio data.

The remaining 92 objects are listed in Table 1. In the first column we give the object's identification; in the second one the related population template (Sect. 3); in the third and fourth columns the morphological type and absolute magnitude, respectively. Columns 5 to 7 list different sources of reddening which were taken into account (Sect. 3). We have also included in the present analysis the spectra of the LMC H II regions NGC 1714, NGC 1895, NGC 2070, and of the SMC H II region N 88 (Henize 88) from BA 86a.

Objects for which a CCD spectrum is available in the near-infrared are labeled with IR in Column 8. We also provide in Column 8, some references corresponding to previous observations of the object.

The stellar population subtraction, the deblending procedure and the line measurements (Sects. 3 and 4) were carried out with a spectral analysis package developed in Porto Alegre.

3. The underlying population and its subtraction

The stellar content in each galaxy must be carefully taken into account in order to study the pure emission component. As well, all sources of reddening extrinsic to the line-emitting region itself must be corrected. The foreground reddening due to our Galaxy was corrected in BA 86a, and BA 87b using a cosec law (Column 5 of Table 1). Additional reddening corrections arising from inclination effects in spirals are from BA 86b and BA 87a and are listed in Column 6.

Guided by measurements of the major absorption features present in each spectrum, we have then subtracted an absorption template built from star cluster spectra, according to the stellar population synthesis method described in Bica (1988). The respective model templates are listed in Column 2 of Table 1. We emphasize that using templates built from star cluster spectra ensures that the subtraction will not be affected by weak underlying emissions, as could be the case using real galaxy templates. For some of the objects, it was necessary to apply a further reddening correction in order to adjust the galaxy continuum to the template. We point out that a difference between the continuum distribution of a given galaxy and its template could also arise from a departure of the population model from the real galaxy. However, in general a simple reddening correction is sufficient to explain the difference. Anyway, these reddening corrections are very small (Column 7 in Table 1).

The great importance of a consistent stellar population subtraction is demonstrated in Figs. 1 to 3. We show in Fig. 1a the effect of subtracting from the galaxy NGC 4438 which presents a suspected Hβ emission, its red model template (S3). Notice how the originally marginal Hβ emission is enhanced after the subtraction. In Fig. 1b we illustrate the subtraction from the NGC 7552 spectrum of its blue model template (S7); notice that without the subtraction, an error of about 40% on the Hβ line intensity would arise which would in turn affect considerably the Hα/Hβ ratio, implying a large error in the reddening determination. Figures 2a and 2b show the effect of the subtraction in the Hα + [N II] $\lambda\lambda$ 6548,84 region for NGC 4438 and NGC 5064 respectively. For NGC 4438 the effect on Hα of the subtraction is negligible, while for a weaker case like NGC 5064 it becomes fundamental as after the subtraction, Hα shows up more prom-

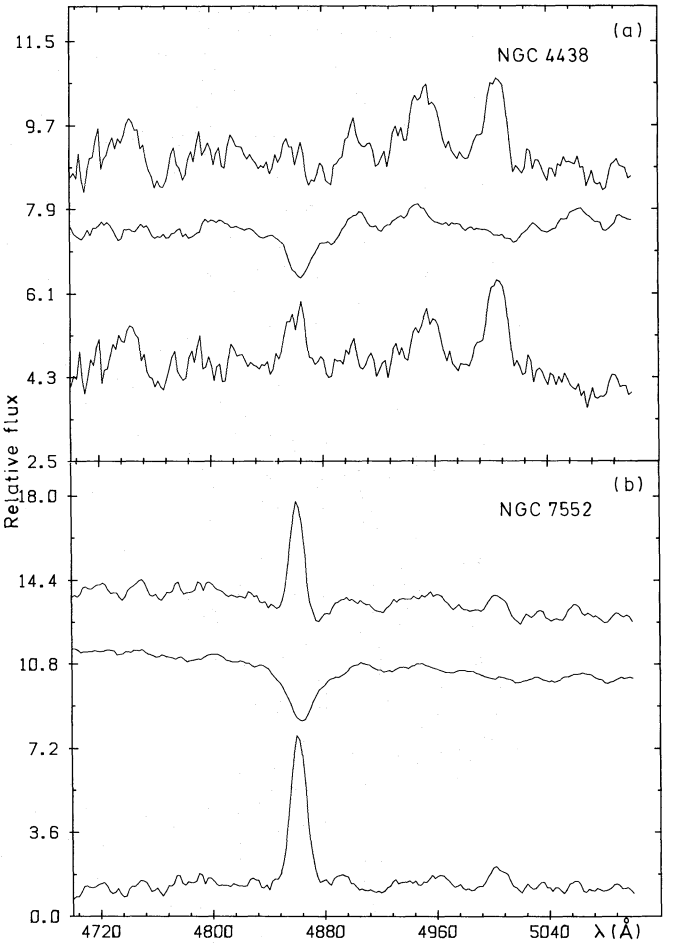

Fig. 1a and b. Subtraction of the population template in the Hβ, [O III] region. The upper spectrum is the composite *observed* spectrum (stellar population plus emission spectrum). The medium spectrum represents the model stellar population corresponding to this object, the lower spectrum is the pure emission spectrum. **a** Galaxy with its red model population. **b** Galaxy with its blue model population. Vertical units correspond to $F_\lambda(5870\,\text{Å}) = 10$ in the composite observed spectrum; a suitable constant was added to some of the spectra for ease of visualization

Table 1. Properties of the galaxy sample

(1) Object	(2) Template	(3) Mtype	(4) M_B	(5) $E(B-V)$g	(6) $E(B-V)$i	(7) $E(B-V)$p	(8) Comments
N 88	–	–	–	0.03	–	–	SMC H II region, 8
NGC 289	S3	Sc	−21.41	0.0	0.10	0.0	1
NGC 625	–	Am	−17.33	0.0	–	–	6
NGC 692	S3	Sc	−22.96	0.0	–	0.0	
NGC 772	S4	Sb	−23.29	0.02	0.19	0.08	1, 3, 4
NGC 908	S4	Sc	−22.15	0.0	0.11	0.06	1
NGC 986*	S7	Sb	−21.81	0.0	–	0.0	1
NGC 1084	S6	Sc	−21.62	0.0	0.0	0.04	1, 3
NGC 1316	S2	Sa	−23.08	0.0	–	0.10	1, 7
NGC 1353	S4	Sc	−20.75	0.0	0.02	0.0	
NGC 1371	S2	Sa	−20.76	0.0	0.0	0.02	
NGC 1380	S1	Sa	−21.30	0.0	0.0	0.04	1, 7
NGC 1400	E2	S0	−17.94	0.0	–	0.20	
IC 1459	E1	E	−21.61	0.0	–	0.04	1, 7
NGC 1553	E5	S0	−21.26	0.01	–	0.05	1, 7
NGC 1637	S4	Sc	−19.72	0.03	–	0.02	3
NGC 1714	–	–	–	0.06	–	–	IR, LMC H II region, 10
NGC 1895	–	–	–	0.06	–	–	IR, LMC H II region,
NGC 2070	–	–	–	0.06	–	–	IR, LMC H II region, 9
NGC 2442*	S4	Sc	−21.20	0.06	–	0.04	IR, 1
NGC 2903	S7	Sc	−20.96	0.01	0.18	0.08	3
NGC 2997	S5	Sc	−21.40	0.08	–	0.0	IR, 1
NGC 3054	S3	Sc	−21.46	0.05	0.02	0.02	IR, 1
NGC 3056	E4	S0	−18.36	0.06	–	0.0	IR
NGC 3351	S5	Sb	−20.66	0.0	0.0	0.0	3
NGC 3358	S3	Sa	−21.69	0.06	0.06	0.0	IR, 1
NGC 3368	S3	Sb	−21.41	0.0	0.36	0.0	1, 3, 4
NGC 3623	S3	Sa	−21.48	0.0	0.25	0.0	1, 4
NGC 3627	S4	Sb	−21.48	0.0	0.11	0.02	1, 3, 4
NGC 3783	–	Sa	−20.81	0.05	–	0.0	Seyfert 1, 13, 14
NGC 3887	S4	Sb	−20.32	0.01	–	0.0	IR
NGC 4027	S7	Sc	−21.06	0.02	–	0.0	1
NGC 4038	S5	Sc	−21.40	0.01	0.08	0.04	1, 5
NGC 4039	S6	Sc	−19.43	0.01	0.04	0.04	5
NGC 4192	S3	Sb	−21.85	0.0	0.49	0.0	1, 4
NGC 4254	S4	Sc	−21.59	0.0	–	0.0	1
IC 4296	E5	E	−22.72	0.04	–	0.08	IR, 7
NGC 4303	S6	Sc	−21.84	0.0	–	0.06	1
NGC 4321	S5	Sc	−21.91	0.0	–	0.09	1
IC 4329A	–	Sa	−21.70	0.03	0.79	0.0	IR, Seyfert 1, 11, 12, 13, 14
NGC 4374	E5	E	−21.47	0.0	–	0.04	1
NGC 4435	E2	S0	−19.98	0.0	–	0.0	
NGC 4438	S3	Sb	−21.73	0.0	0.39	0.0	1, 4
NGC 4476	E4	E	−18.62	0.0	–	0.05	
NGC 4486	E1	E	−22.08	0.0	–	0.0	1, 2
NGC 4501	S3	Sc	−21.93	0.0	0.18	0.02	1, 4
NGC 4507	S3	Sb	−21.96	0.05	–	0.06	Seyfert 2, 6
NGC 4535	S7	Sc	−21.58	0.0	0.19	0.06	1
NGC 4536	S5	Sc	−22.15	0.0	0.23	0.02	1
NGC 4548	S2	Sb	−21.27	0.0	–	0.09	1
NGC 4569	S7	Sb	−22.31	0.0	0.19	0.10	1, 4
NGC 4579	S3	Sb	−21.69	0.0	–	0.04	1, 4
NGC 4594	S1	Sb	−22.81	0.0	0.04	0.0	1, 2, 3, 4
NGC 4856	S2	Sa	−20.22	0.01	0.01	0.02	IR
IC 4889	E5	S0	−21.36	0.03	–	0.0	IR, 1, 7

Table 1 (continued)

(1) Object	(2) Template	(3) Mtype	(4) M_B	(5) $E(B-V)$g	(6) $E(B-V)$i	(7) $E(B-V)$p	(8) Comments
NGC 4936*	E5	E	−21.65	0.03	–	0.02	IR
NGC 4941	S4	Sb	−20.07	0.0	0.26	0.0	Seyfert 2, 3
NGC 4958	E2	S0	−20.63	0.0	–	0.06	IR
NGC 4981*	S4	Sc	−20.91	0.0	–	0.04	
NGC 5064	S3	Sa	−22.27	0.10	0.22	0.0	IR, 1
NGC 5090	E1	E	−21.37	0.07	–	0.06	1, 7
NGC 5101*	S2	Sa	−21.06	0.02	–	0.08	IR, 1
NGC 5102	E8	S0	−18.73	0.04	–	0.04	IR, 7
NGC 5156	S4	Sc	−21.49	0.11	–	0.25	1
NGC 5236	S7	Sc	−21.12	0.03	–	0.0	IR, 1
NGC 5248	S5	Sc	−21.19	0.0	–	0.04	1, 3
NGC 5253	–	Am	−18.20	0.03	–	0.0	1R, 15
NGC 5266*	E5	S0	−21.92	0.10	–	0.02	IR, 1, 7
IC 5267	S2	Sa	−21.53	0.0	–	0.04	1
IC 5325	S6	Sc	−20.30	0.0	–	0.0	
NGC 5612	S3	Sb	−21.65	0.08	0.17	0.0	IR, 1
NGC 5643	S3	Sc	−21.20	0.09	–	0.0	IR, Seyfert 2, 1, 6, 14
NGC 6215	S6	Sc	−21.33	0.17	–	0.0	1
NGC 6221	S6/S7	Sc	−21.55	0.16	0.27	0.0	Seyfert 2, 1, 14
NGC 6300	S4	Sb	−21.32	0.10	0.26	0.02	Seyfert 2, 1, 6
NGC 6699	S5	Sc	−21.91	0.05	–	0.04	IR
NGC 6744	S3	Sc	−21.98	0.04	0.11	0.05	IR, 1
NGC 6758	E5	E	−21.62	0.04	–	0.10	IR, 7
NGC 6776	E5	E	−22.38	0.04	–	0.0	IR, 7
NGC 6782	S5	Sb	−22.57	0.04	0.01	0.06	IR
NGC 6861	E5	S0	−21.77	0.03	–	0.10	IR, 1, 7
NGC 6868*	E5	S0	−21.92	0.03	–	0.10	IR, 1, 7
NGC 6923	S3	Sc	−21.61	0.02	0.20	0.02	IR, 1
NGC 6925	S3	Sc	−22.37	0.02	0.20	0.0	IR, 1
NGC 6942	S3	Sa	−20.94	0.02	0.11	0.0	IR
NGC 7049	S1	Sa	−21.57	0.01	–	0.15	IR, 1, 7
NGC 7083	S4	Sb	−22.81	0.02	–	0.0	1
NGC 7205	S4	Sb	−21.48	0.01	0.01	0.04	1
NGC 7213	S2	Sa	−21.96	0.0	–	0.0	Seyfert like, 1, 7
NGC 7329	S1	Sc	−22.08	0.01	0.09	0.02	IR
NGC 7392	S5	Sc	−21.73	0.0	0.16	0.04	
NGC 7410	S1	Sa	−22.40	0.0	0.05	0.10	1
NGC 7469	–	Sb	−23.10	0.01	0.02	0.0	Seyfert 1, 13, 14
NGC 7496	S6/S7	Sc	−20.89	0.0	–	0.0	Seyfert 2
NGC 7552	S7	Sc	−21.49	0.0	0.18	0.0	1
NGC 7582	S6/S7	Sb	−21.75	0.0	0.45	0.0	Seyfert 2, 1

Notes to Table 1: Column (1): * in addition to the $E(B-V)$ corrections indicated here, the following spectra had supplementary corrections when the spectral groups were defined in Bica (1988): NGC 986, $E(B-V) = 0.17$; NGC 2442, $E(B-V) = 0.29$; NGC 4936, $E(B-V) = 0.16$; NGC 4981, $E(B-V) = 0.17$; NGC 5101, $E(B-V) = 0.07$; NGC 5266, $E(B-V) = 0.15$; and NGC 6868, $E(B-V) = 0.09$. These additional corrections could be assigned to one or more of the following reasons: a) an atypical dust lane possibly associated with the nucleus; b) the galaxy disc is more inclined than suggested by axial ratio (asymmetries); c) an uncertain cosec law owing to small $|b|$. Column (2): The mixtures of templates are: NGC 6221: (0.5 S6) + (0.5 S7), NGC 7496: (0.3 S6) + (0.7 S7), NGC 7582: (0.35 S6) + (0.65 S7). Column (5): Galactic reddening along the line of sight. Column (6): Reddening due to inclination in spiral galaxies. Column (7): Residual intrinsic reddening. Column (8): Galaxies for which a near-infrared spectrum is available are indicated with IR.

References: (1) Véron-Cetty and Véron, 1986; (2) Heckman, 1980b; (3) Stauffer, 1982b; (4) Keel, 1983; (5) Keel et al., 1985; (6) Phillips et al., 1983; (7) Phillips et al., 1986; (8) Testor and Pakull, 1985; (9) Mathis et al., 1985; (10) Dufour and Harlow, 1977; (11) Pastoriza, 1979; (12) Wilson and Penston, 1979; (13)Martin, 1974; (14) Morris and Ward, 1988; (15) Welch, 1970.

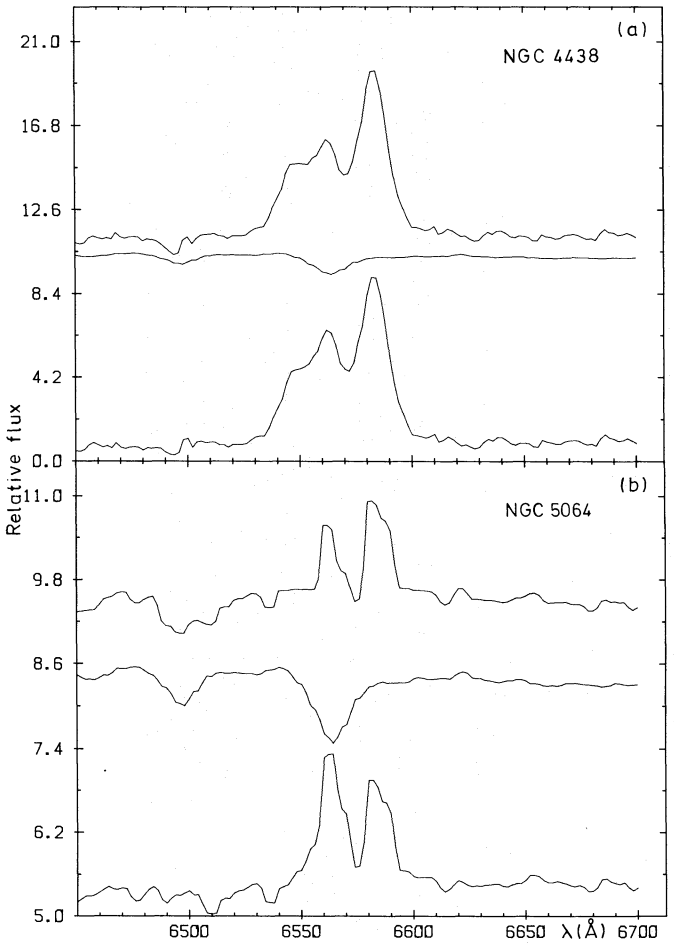

Fig. 2a and b. Subtraction of the population template in the Hα, [N II], [S II] region. Same display as in Fig. 1. **a** Hα is so strong that the population subtraction effect is minor. **b** The subtraction is fundamental. Units as in Fig. 1

inently than [N II] λ 6584. Finally, Fig. 3 depicts the importance of this procedure in the [O I] λ 6300 region, where the TiO band often disturbs the line measurement. Examples of population subtraction for the entire spectrum from 3700 to 9700 Å can be seen in Bica (1988).

4. Line measurements and comparison with previous studies

4.1. Method and results

The measurement of emission line intensities was carried out on the pure emission component, as obtained in Sect. 3. We have used gaussian fitting in all cases, which also allowed us to deblend composite profiles. We show in Table 2 the results for normal H II regions and for the nuclei of the amorphous galaxies NGC 625 and NGC 5253. In Table 3 we have grouped Seyfert-like galaxies and the strong-lined nuclear H II region in NGC 5236. In Table 4 we present the results for the narrow line region in Seyfert 1 nuclei. Finally, we group in Table 5 the remaining galaxies with a weaker emission component. In all tables the intensities are normalized to $I(\mathrm{H}\alpha) = 100$. The relative importance of the emission component with respect to the stellar population non-subtracted spectrum is given by the equivalent width of Hα. In fact, we defined $W^*(\mathrm{H}\alpha)$ as the ratio of $I(\mathrm{H}\alpha)$, the emission in the population subtracted spectrum, to $F_\lambda(5870\,\text{Å})$ in the original spectrum.

The near-infrared spectrum also covers the Hα + [N II] + [S II] region. The agreement between line measurements from IDS and CCD spectra was in general excellent, so we only present the average values in the tables. As a comparison we show explicitly both measurements for some galaxies (e.g. NGC 5236). In one case however, NGC 2997, the difference is considerable (Table 5). We assign this difference to a strong spatial dependence of the emission spectrum in the central region of this galaxy. A cross attached to the object's identification in Tables 2 to 5 indicates that the results are from CCD spectra. In Tables 3 and 4 containing objects where broad lines are also present, we consider the narrow component *n* of Hα as the reference line. In all cases we use the theoretical intensity ratios [O III] λ 5007/[O III] λ 4959 = 2.98 and [N II] λ 6584/[N II] λ 6548 = 2.97 as a constraint in the deblends. We only list the strongest component in the tables. The [S II] lines in some cases could not be deblended, then a tilda has been put in the λ 6717 column while the total flux is given in the λ 6731 column. Examples of the deblending procedure are given for different lines with various levels of intensity in Figs. 4 to 8. Notice that the vertical units are defined in terms of $F_\lambda(5870\,\text{Å}) = 10$ for the composite stellar plus emission spectra, allowing a direct comparison of galaxies among the figures.

The model template for each galaxy had been previously established according to the spectral groups in Bica (1988). We have determined the underlying template population for Seyfert nuclei (Table 1) from the equivalent widths of strong absorption lines and guided by the most probable population according to the morphological type of the host galaxy (Bica, 1988). Out of eight nuclei indicated as Seyfert 2 or Seyfert-like in Column 8 of Table 1, three have a blue underlying stellar population and five have red template populations. For all these objects it was not necessary to include a power-law in addition to the stellar population to reproduce the observed continuum, in the

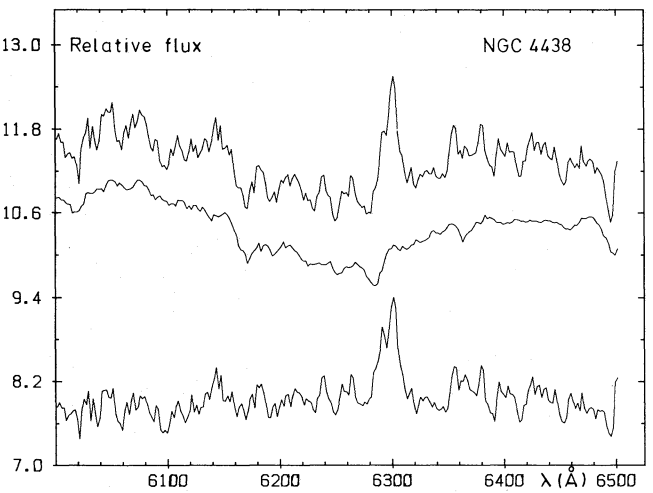

Fig. 3. Subtraction of the population template in the [O I] λ 6300 region. Same display as in Fig. 1. The TiO band must, as a rule, be taken into account. Units as in Fig. 1

Table 2. Emission-line intensities for H II regions and amorphous galaxies

(1)	(2) N 88	(3) N 625	(4) N 1714	(5) N 1895	(6) N 2070	(7) N 5253	(8) N 5253+
$W^*(H\alpha)$	1228	1213	1303	588.7	1455	595	685
[O II] λ 3727	5.7	87.3	24.6	57.3	61.3	36.5	–
[Ne III] λ 3869	9.1	11.0	5.7	4.8	4.0	8.1	–
H8 + He I λ 3888	2.4	6.7	4.2	–	2.0	2.3	–
[Ne III] λ 3968	5.4	10.2	4.8	–	2.8	5.1	–
He I λ 4026	0.2	–	0.6	–	–	–	–
Hδ	4.5	6.6	4.7	4.8	3.2	4.1	–
Hγ	9.9	15.9	10.5	13.1	7.4	10.3	–
[O III] λ 4363	2.8	2.1	1.5	–	1.1	1.7	–
He I λ 4471	1.0	1.6	1.1	–	0.6	1.3	–
Hβ	27.8	30.8	29.6	28.2	26.6	24.6	–
[O III] λ 5007	191.8	143.9	121.7	84.0	114.3	139.8	–
He I λ5876	3.3	4.1	3.2	3.5	3.0	3.4	–
[O I] λ 6300	0.2	0.5	0.4	–	0.1	0.6	–
[S III] λ 6312	0.7	0.6	0.5	–	0.5	0.8	–
Hα	100.0	100.0	100.0	100.0	100.0	100.0	100.0
[N II] λ 6584	5.4	7.5	4.0	9.0	4.5	8.9	10.5
He I λ 6678	1.0	1.0	1.0	0.6	1.3	1.3	1.5
[S II] λ 6717	0.8	4.5	1.8	4.3	2.2	5.4	7.1
[S II] λ 6731	1.1	3.6	1.7	2.9	2.2	4.7	6.1
He I λ 7065	3.3	0.9	1.0	–	0.9	1.5	2.0
[Ar III] λ 7135	3.0	4.6	4.2	3.8	3.9	4.0	5.7
He I λ 7280	0.2	–	0.2	–	–	0.3	0.3
[O II] λ 7319	0.8	0.9	–	–	0.5	1.5	1.4
[O II] λ 7330	0.8	1.0	0.9	–	0.6	0.7	1.2
[Ar III] λ 7751	0.7	–	0.9	–	1.0	0.9	1.5
[S III] λ 9069	–	–	10.5	9.7	–	–	13.7
[S III] λ 9532	–	–	30.1	20.2	–	–	28.2

Notes to Table 2: N88 is Henize 88, other N numbers correspond to NGC numbers; $W^*(H\alpha)$ in Å; the CCD spectrum of NGC 5253 is indicated by a cross; [O II] λ 3723 line intensities for N 88 and NGC 2070 are respectively from Testor and Pakull (1985) and Mathis et al. (1985).

3700–9600 Å range. For NGC 7213 however, when data in the near-UV is added, there is evidence for a power-law continuum contribution (Halpern and Filippenko, 1984). For the three Seyfert 1 nuclei in Table 1, a non-thermal contribution is important. The choice of the underlying stellar population model becomes extremely uncertain. But using for NGC 3783 and NGC 7469 absorption lines in the visible and for IC 4329 Å additional information from the near-infrared range, we found that a red population is suitable and thus we have adopted template S2. The resulting contributions from the stellar component at λ 5870 Å are: (45 ± 15)%, (50 ± 15)% and (30 ± 10)% for, respectively, NGC 3783, NGC 7469 and IC 4329 Å. We illustrate this result for the near-infrared region in IC 4329 A (Fig. 9). Notice the Ca II triplet from the stellar population superimposed on strong emission features which could be assigned to Ca II in emission and/or to blended high order broad hydrogen Paschen lines as well as permitted neutral oxygen.

4.2. *Comparison with previous studies*

In view of such comparisons, we provide in Column 9 of Table 1 a non-exhaustive list of references corresponding to previous emission line studies for galaxies in our sample. Although many objects have been observed already, the data differ through the instrumentation, the spectral resolution and range, as well as through the processing (reddening correction, stellar population subtraction, line deblending . . .). In the following analysis, we have excluded Seyfert 1 nuclei owing to possible intrinsic line variations.

We compare in Fig. 10 line ratios from our data to those obtained by Keel (1983) and Keel et al. (1985) for objects in common: 10 galaxies at low or moderate emission level (0.9 Å < $W^*(H\alpha)$ < 9 Å) and 2 objects with $W^*(H\alpha) \simeq 70$ Å. We compare line ratios which are essentially reddening independent. The line-ratios [N II λ 6584/Hα (Fig. 10a) agree within 20% and other-line ratios show an equally good agreement (Fig. 10b) but for 2 departing points in the case of [S II]/Hα, a line-ratio which may be quite dependent on the slit position. The good correlations observed even for weak lines certainly reflect the fact that in both studies, stellar populations have been subtracted, although, Keel had derived population templates using a stellar library.

We confront in Fig. 11, our results to those by Phillips et al. (1986) for common galaxies. The latter study is restricted to the

Table 3. Emission-line intensities for Seyfert 2 and other strong-lined galaxies

(1)	(2) N 4507	(3) N 4941	(4) N 5236	(5) N 5236+	(6) N 5643	(7) N 5643+	(8) N 6221	(9) N 6300	(10) N 7213	(11) N 7496	(12) N 7582
W^*(Hα)n	52.0	15.4	41.1	45.0	33.8	33.9	80.4	5.1	15.0	76.8	64.4
[O II] λ 3727	64.3	–	12.3	–	60.7	–	22.1	183.5	25.8	29.1	31.2
[Ne III] λ 3869	28.0	–	–	–	35.7	–	9.7	–	–	–	11.4
[Ne III] λ 3968	13.4	–	9.0	–	5.0	–	–	–	–	–	10.4
[S II] λ 4072	4.4	–	–	–	–	–	–	–	8.3	–	–
Hδ	7.3	–	9.2	–	–	–	11.1	–	11.7	8.2	11.8
Hγ	15.1	27.4	15.8	–	8.4	–	11.0	–	22.2	8.9	16.1
[O III] λ 4363	6.8	–	–	–	3.4	–	–		8.9	–	
He II λ 4686	3.8	–	–	–	5.3	–	–	–	–	–	4.1
(Hβ)n	37.7	29.3	29.8	–	16.0	–	23.6	18.3	16.1	27.1	27.8
(Hβ)b	–	–	–	–	–	–	9.0	–	117.8	–	–
[O III] λ 5007	285.2	271.0	5.3	–	241.9	–	16.1	297.4	67.7	18.8	64.7
[N I] λ 5198	2.2	–	–	–	8.9	–	–	–	–	–	–
He I λ 5876	5.9	–	–	–	–	–	–	–	–	6.1	–
[O I] λ 6300	16.1	27.1	–	–	18.3	–	2.5	48.6	53.8	7.7	2.7
[O I] λ 6364	6.4	–	–	–	7.5	–	0.8	–	14.3	–	–
[Fe X] λ 6375	1.9	–	–	–	–	–	–	–	–	–	–
(Hα)n	100.0	100.0	100.0	100.0	100.0	100.0	100.0	100.0	100.0	100.0	100.0
(Hα)b	85.5	–	–	–	–	–	35.4	–	317.9	–	–
[N II] λ 6584	42.4	150.0	49.9	48.5	100.3	113.0	52.9	196.9	27.5	46.2	69.1
He I λ 6678	8.4	–	–	–	–	–	–	–	–	–	–
[S II] λ 6717	19.7	35.2	10.5	11.7	31.2	34.9	10.3	45.4	13.2	15.0	12.1
[S II] λ 6731	26.8	36.9	10.9	11.8	33.3	34.2	12.4	51.2	11.5	12.1	15.3
[Ar III] λ 7135	7.3	–	–	–	–	8.6	–	–	–	–	–
[O I] λ 7319	–	–	–	–	–	2.8	–	–	13.2	–	–
[O II] λ 7330	9.9	–	–	–	–	4.6	–	–	–	–	–
[Ar III] λ 7751	–	–	–	–	–	1.7	–	–	–	–	–
[S III] λ 9069	–	–	–	5.8	–	26.3	–	–	–	–	–
[S III] λ 9532	–	–	–	13.8	–	65.5	–	–	–	–	–

Notes to Table 3: N numbers stand for NGC numbers. W^*(Hα) as in Table 2. CCD spectra are indicated by crosses. The line intensities are relative to the narrow component of Hα.

Hα, [N II] region and we find an agreement better than 25%. This comparison is particularly important because it includes measurements reaching down a detection level as low as $W^*(\text{H}\alpha) \simeq 0.5$ Å and with a maximum value of 2.5 Å. Phillips et al. (1986) had also subtracted a stellar population.

We compare in Fig. 12, our line measurements to those derived by Véron-Cetty and Véron (1986). We have many objects in common (Table 1). However, most of their line intensities must be considered as lower limits as they have not subtracted the underlying stellar population. We have displayed in Fig. 12 only measures which are not lower limits in their study: consequently we are left with strong-lined nuclei and/or the strong lines in low-level emission nuclei ($W^*(\text{H}\alpha) > 3$ Å). The agreement is in general better than 30%; a large part of the scatter may be due to the stellar population contamination in their data. Remember from Figs. 1 to 3, the importance of using the appropriate population model if one wishes to disentangle the emission and absorption Hβ components or access weak lines which otherwise are drowned in the underlying stellar population.

Last, a comparison is shown in Fig. 13 with data by Morris and Ward (1988), excluding Seyfert 1 nuclei. The objects in common are the strong-lined objects NGC 5643 and NGC 6221 ($W^*(\text{H}\alpha) > 30$ Å). This comparison is important because their data are of high quality throughout the whole optical range (IPCS and CCD detectors). They do not subtract the stellar population but its effect should be minor as the emission component largely dominates for galaxies in this sample. They also do not deblend the lines, so we have merged out Hα and [N II] line measurements and have used this as a normalization. In order to test the instrumental response calibration, we compare lines over the entire spectral range and have had to apply to Morris and Ward's data the same reddening corrections as to ours. In the case of strong lines the agreement is better than 5%. For weak lines it is in the 10 to 20% range, possibly degraded by some residual stellar population contamination in their data or by a larger error on the instrumental response at [O II] λ 3727 in IDS data.

Overall, these confrontations are satisfactory and demonstrate that such line measurements can be trusted within an accuracy of 20%. Let us now turn to the analysis of the physical properties of the gas in galaxies from our sample.

Table 4. Emission-line intensities for Seyfert 1 galaxies. Same conventions as in Table 3

(1)	(2) NGC 3783	(3) IC 4329A	(4) IC 4329A +	(5) NGC 7469	(1)	(2) NGC 3783	(3) IC 4329A	(4) IC 4329A +	(5) NGC 7469
W^*(Hα)n	82.2	15.6	20.5	41.1	(He I λ 5876)b	40.6	208.9	–	43.7
[O II] λ 3727	14.4	–	–	39.1	[Fe VII] λ 6087	9.0	41.2	–	6.6
[Ne III] λ 3869	86.6	–	–	–	[O I] λ 6300	8.1	–	10.6	7.7
[Ne III] λ 3968	33.4	–	–	11.7	[O I] λ 6364	2.7	–	3.5	5.0
Hδ	61.3	81.4	–	28.5	[Fe X] λ 6375	4.6	–	4.0	–
(Hγ)n	19.6	40.1	–	10.6	(Hα)n	100.0	100.0	100.0	100.0
(Hγ)i	95.3	191.5	–	26.1	(Hα)i	845.2	1774.4	1424.2	379.0
(Hγ)b	–	–	–	20.9	(Hα)b	200.4	836.8	504.6	295.5
[O III] λ 4363	5.0	35.4	–	6.7	[N II] λ 6584	17.7	16.7	17.6	58.6
He II λ 4686	10.6	–	–	7.7	[S II] λ 6717	7.3	–	13.5	11.4
(Hβ)n	34.2	16.4	–	16.0	[S II] λ 6731	6.8	–	12.3	16.3
(Hβ)i	203.5	287.1	–	76.2	(He I λ 7065)n	3.4	–	3.4	–
(Hβ)b	153.2	262.9	–	120.1	(He I λ 7065)b	19.4	–	18.6	–
[O III] λ 5007n	188.1	236.1	–	97.2	[Ar III] λ 7135	7.6	–	4.7	–
[O III] λ 5007b	52.8	–	–	49.1	[O II] λ 7319	8.2	–	2.0	–
[Fe XIV] λ 5303	8.5	–	–	–	[O II] λ 7330	–	–	2.7	–
[Fe VII] λ 5721	4.6	–	–	7.4	[S III] λ 9069	–	–	17.2	–
(He I λ 5876)n	7.7	62.0	–	8.9	[S III] λ 9532	–	–	42.1	–

Table 5. Emission-line intensities for weak-lined galaxies. Same conventions as in Table 3

(1) Object	(2) W^*(Hα)	(3) [O II]	(4) Hδ	(5) Hγ	(6) Hβ	(7) [O III]	(8) [O I]	(9) Hα	10) [N II]	(11) [S II] 6717	(12) [S II] 6731
NGC 289	7.5	–	–	–	–	–	–	100	72.3	~	42.4
NGC 692	4.4	–	–	–	–	–	–	100	139.2	~	48.4
NGC 772	1.5	–	–	–	–	–	–	100	112.7	90.3	72.5
NGC 908	11.7	–	–	–	–	–	–	100	55.8	–	–
NGC 986	52.5	–	–	14.7	24.5	4.7	–	100	50.5	10.2	9.9
NGC 1084	18.4	–	–	–	13.2	–	–	100	40.4	17.0	20.2
NGC 1316	1.3	–	–	–	–	–	–	100	161.4	~	135.3
NGC 1353	4.3	–	–	–	44.5	–	–	100	70.2	–	–
NGC 1371	2.2	–	–	–	–	–	–	100	94.1	~	134.4
NGC 1380	1.4	–	–	–	–	–	–	100	73.0	–	–
NGC 1400	1.5	–	–	–	–	–	–	100	93.5	–	–
IC 1459	2.6	149.9	–	–	54.5	113.6	–	100	246.5	65.9	52.1
NGC 1553	0.5	–	–	–	–	–	–	100	304.6	–	–
NGC 1637	32.6	–	–	–	10.2	–	–	100	69.3	15.2	21.3
NGC 2442	3.8	–	–	–	–	33.4	–	100	186.9	70.1	67.0
NGC 2903	27.9	–	9.4	20.5	27.0	–	–	100	42.7	12.3	12.5
NGC 2997	11.8	–	–	–	22.0	–	–	100	39.8	~	16.8
NGC 2997 +	3.6	–	–	–	–	–	–	100	251.0	46.1	46.4
NGC 3054	0.5	–	–	–	–	–	–	100	266.9	132.2	87.3
NGC 3056	3.2	–	–	–	–	–	–	100	47.6	39.4	38.0
NGC 3351	14.0	–	–	–	21.2	–	–	100	39.7	~	25.4
NGC 3358	1.3	–	–	–	–	–	–	100	150.7	38.0	37.7
NGC 3368	1.4	–	–	–	–	–	–	100	176.9	~	143.6
NGC 3623	2.0	–	–	–	–	–	–	100	120.2	~	57.0
NGC 3627	0.9	–	–	–	–	158.7	–	100	308.0	~	268.6

Table 5 (continued)

(1) Object	(2) $W^*(H\alpha)$	(3) [O II]	(4) Hδ	(5) Hγ	(6) Hβ	(7) [O III]	(8) [O I]	(9) Hα	10) [N II]	(11) [S II] 6717	(12) [S II] 6731
NGC 3887	7.4	–	–	–	–	–	–	100	58.2	21.5	22.0
NGC 4027	20.0	–	–	–	23.7	–	–	100	39.9	17.7	16.8
NGC 4038	57.6	11.5	4.7	8.1	23.3	5.4	2.3	100	45.6	18.9	12.7
NGC 4039	88.3	46.0	–	7.3	26.1	21.8	6.8	100	41.5	21.3	17.5
NGC 4192	5.1	114.6	–	–	–	–	–	100	83.4	36.5	36.6
NGC 4254	8.7	–	–	–	24.3	12.8	–	100	57.6	~	29.2
IC 4296	1.1	–	–	–	–	–	–	100	176.0	45.9	54.2
NGC 4303	14.8	17.9	–	–	17.6	15.2	6.1	100	63.6	~	34.1
NGC 4321	8.6	25.6	–	–	15.6	7.1	–	100	84.8	~	43.0
NGC 4374	2.0	–	–	–	–	–	–	100	117.8	~	52.1
NGC 4435	2.0	–	–	–	–	–	–	100	59.6	~	55.9
NGC 4438	9.1	81.0	–	–	22.4	35.7	16.4	100	141.0	63.6	51.4
NGC 4476	1.9	–	–	–	–	–	–	100	59.1	–	–
NGC 4486	6.7	72.8	–	19.7	25.1	36.1	–	100	138.8	50.0	33.8
NGC 4501	3.2	–	–	–	–	111.5	–	100	158.1	48.8	41.5
NGC 4535	33.7	–	–	23.0	29.1	–	–	100	41.6	11.5	10.7
NGC 4536	38.8	22.9	–	5.3	17.2	8.5	3.3	100	42.1	19.0	13.3
NGC 4548	2.6	–	–	–	–	–	–	100	95.6	32.4	36.4
NGC 4569	6.8	139.9	–	–	22.6	23.3	–	100	104.8	26.1	28.0
NGC 4579	4.1	77.9	–	–	55.1	51.3	49.2	100	287.3	~	183.6
NGC 4594	1.5	–	–	–	–	–	–	100	281.6	50.4	57.9
NGC 4856	2.9	–	–	–	–	–	–	100	51.5	25.4	30.5
IC 4889	0.6	–	–	–	–	–	–	100	325.6	–	–
NGC 4936	3.8	195.0	–	–	–	–	–	100	110.5	59.8	45.1
NGC 4958	0.8	–	–	–	–	–	–	100	189.0	45.5	61.1
NGC 4981	10.0	–	–	–	16.3	–	–	100	48.3	18.4	16.3
NGC 5064	2.2	–	–	–	–	–	–	100	105.1	~	46.1
NGC 5090	2.2	–	–	–	–	–	–	100	104.4	–	–
NGC 5101	2.0	–	–	–	45.2	162.6	–	100	184.6	56.3	46.2
NGC 5102	0.6	–	–	–	–	–	–	100	84.3	~	207.6
NGC 5156	2.4	–	–	–	–	–	–	100	126.7	30.2	35.2
NGC 5248	6.1	–	–	–	–	–	–	100	69.2	~	26.6
NGC 5266	2.6	235.0	–	–	–	–	–	100	202.3	87.3	90.6
IC 5267	2.3	–	–	–	–	–	–	100	133.0	~	134.6
IC 5325	8.5	–	–	–	–	–	–	100	70.7	30.2	27.2
NGC 5612	1.0	–	–	–	–	–	–	100	214.9	39.9	42.6
NGC 6215	52.8	7.8	–	3.1	16.5	5.0	–	100	42.8	15.3	11.0
NGC 6699	5.6	–	–	–	–	–	–	100	58.4	10.6	7.3
NGC 6744	1.6	–	–	–	–	–	–	100	125.6	36.8	30.8
NGC 6758	1.5	–	–	–	–	–	–	100	103.2	49.3	43.4
NGC 6776	1.2	–	–	–	–	–	–	100	226.7	93.1	92.2
NGC 6782	5.4	–	–	–	–	–	–	100	63.6	21.0	22.9
NGC 6861	2.2	–	–	–	–	–	–	100	74.6	–	–
NGC 6868	2.3	–	–	–	32.7	39.9	–	100	253.1	71.3	69.9
NGC 6923	1.0	–	–	–	–	–	–	100	219.9	56.7	59.1
NGC 6925	1.0	–	–	–	–	–	–	100	175.7	74.3	53.5
NGC 6942	1.4	–	–	–	–	–	–	100	191.5	46.3	50.7
NGC 7049	1.6	–	–	–	–	–	–	100	176.6	28.9	27.1
NGC 7083	2.5	–	–	–	–	–	–	100	128.0	–	–
NGC 7205	4.2	–	–	–	–	–	–	100	52.2	–	–
NGC 7329	1.1	–	–	–	–	–	–	100	225.1	71.1	67.1
NGC 7392	6.0	–	–	–	–	–	–	100	69.8	~	58.2
NGC 7410	2.4	214.7	–	–	–	95.2	–	100	156.1	~	103.1
NGC 7552	43.9	11.9	5.0	7.4	20.4	3.6	–	100	62.3	11.8	11.9

Note to Table 5: A tilde in column 11 is given when it was not possible to deblend the [S II] $\lambda\lambda$ 6717, 31 pair

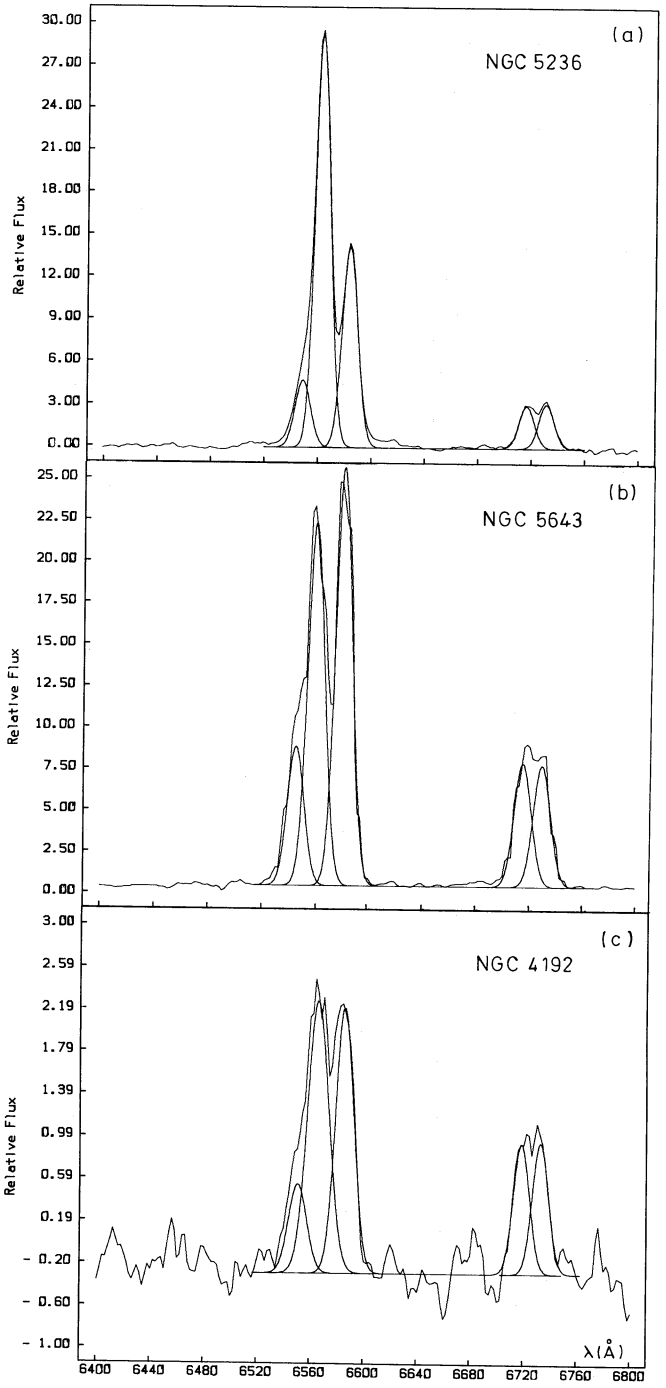

Fig. 4a–c. The deblending in the Hα, [N II], [S II] region for different emission levels and relative intensities. Units as in Fig. 1

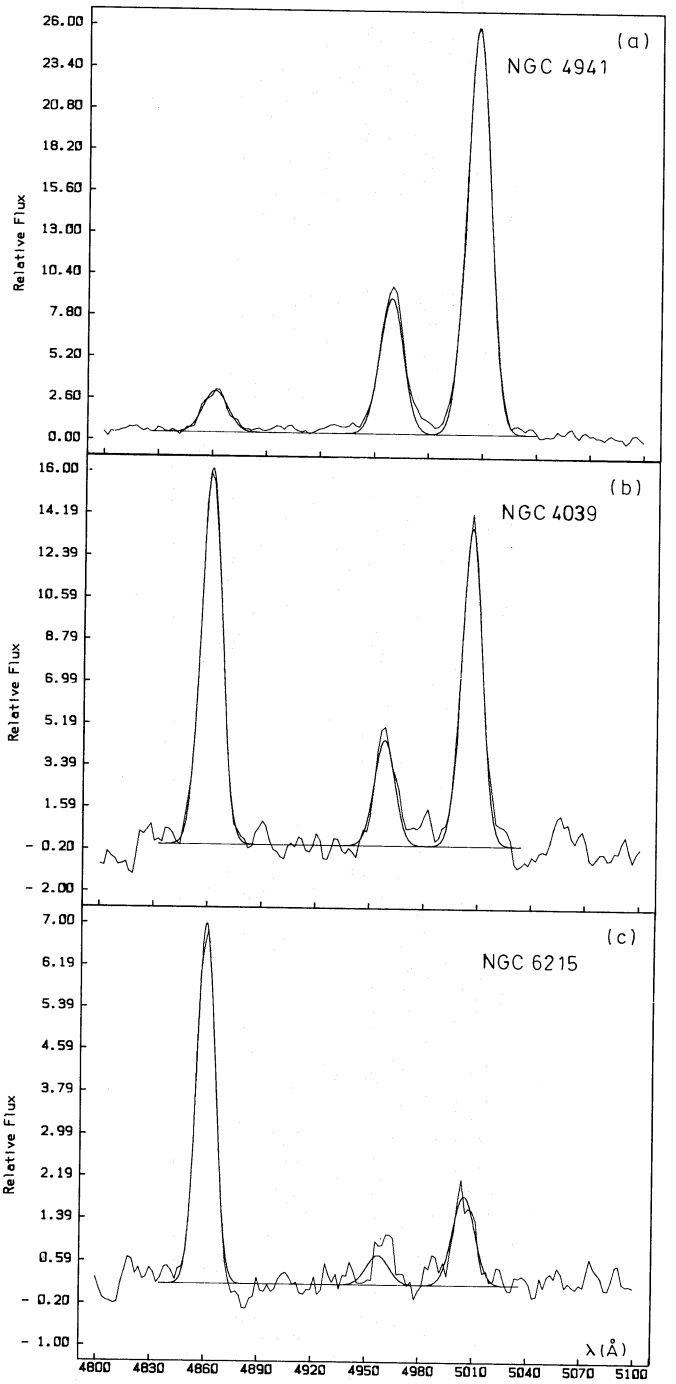

Fig. 5a–c. The gaussian fits in the Hβ, [O III] region for different emission levels and relative intensities. Units as in Fig. 1

5. Physical properties of the gas in a sample of 92 galaxies

5.1. The [N II]/Hα line ratio: metallicity or excitation effect?

We study the properties of the emission component with respect to the host galaxy morphological type and underlying population using the [N II] λ6584 line which is observed in all objects from our sample. We show in Fig. 14a, [N II]/Hα histograms for the galaxies separated according to morphological types and in Fig. 14b, comparative histograms for amorphous galaxies, H II regions and Seyfert galaxies. We conclude that for all morphological types there is a wide range of values of the [N II]/Hα line ratio. We have displayed in Fig. 15 the same line ratio in galaxies separated according to their underlying model population template. For the underlying populations S1, S2, E1, E2 and E5 which correspond to an equally high metallicity (Bica, 1988), the range of [N II]/Hα values is still broad. We recall that in this

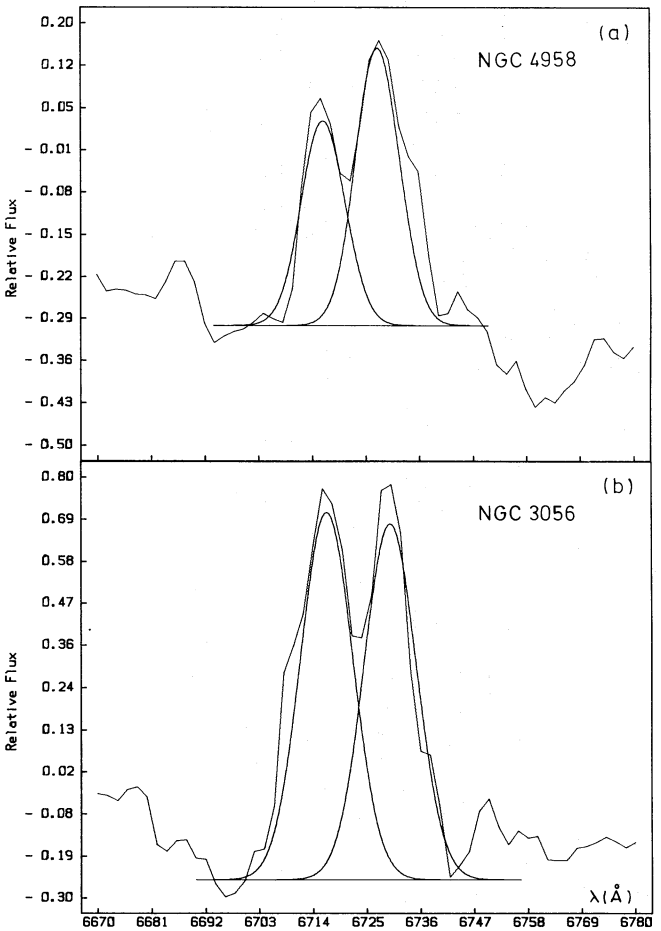

Fig. 6a and b. The gaussian fits in the [S II] region, for different emission levels and relative intensities. Units as in Fig. 1

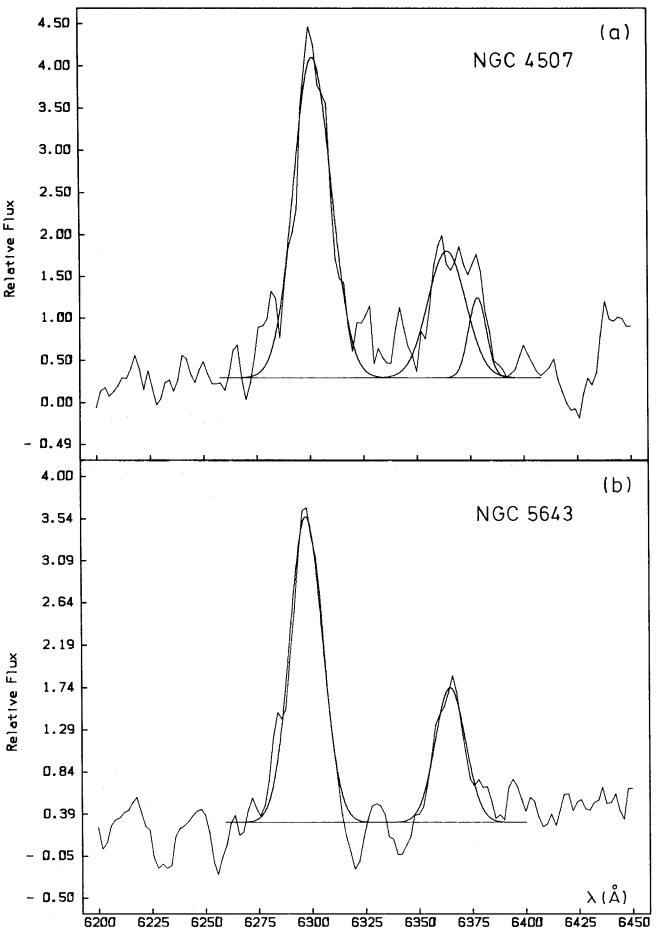

Fig. 7a and b. The gaussian fits in the [O I], [Fe X] region. Units as in Fig. 1

series of papers, $(Z/Z_{\odot}]$ stands for the global metallicity which is mainly represented by the iron-peak elements. As the metallicity is essentially the same in these objects we conclude that there is a wide range in excitation among them. A solar or slightly above solar metallicity is encountered in groups S3, S4, S5, S6 and S7. The [N II]/Hα line ratio in objects with underlying populations S3, S4, shows as well a wide range in excitation. However for groups S5, S6 and S7 this ratio is systematically shifted towards lower values (higher excitation) as is the case for the H II regions in Fig. 14b. In fact, the stellar populations in groups S5 to S7 are considerably bluer than in groups S1 to S4 and their population synthesis indeed requires very young components (Bica, 1988). Groups E4 and E8 correspond to low luminosity metal poor stellar populations (Bica, 1988) and the low [N II]/Hα values encountered in objects with such underlying populations could be assigned to both excitation and low metallicity.

It can also be concluded from the comparison between Figs. 14a and 15 that the underlying population in the nuclear region bears more relationship to the gas component than the morphological type of the host galaxy does.

The [S II] λλ 6717, 31 lines are measured for 88% of the objects in our sample (Tables 2 to 5). We show in Fig. 16 the relationship between line ratios [S II]/Hα and [N II]/Hα. There is a good correlation, thus suggesting that the above conclusions for [N II] are also valid for the [S II] lines. However some scatter is present which could arise from a different dependence of one of the ions on metallicity or excitation (Phillips et al., 1986). Indeed, there is observational evidence that excitation can explain much of the enhancement of the [N II]/Hα ratio in spiral nuclei (Pagel, 1983).

We show in Figs. 17a and 17b respectively the [N II]/Hα and [S II]/Hα line ratios vs total galaxy magnitude M_B. The SMC and LMC H II regions have been included as well. There is a trend with M_B, although at constant high luminosity there is a considerably scatter in the line ratios.

In Figs. 18a and 18b the same line ratios are plotted against the sum of the equivalent widths of the best metallicity indicators in the visible spectrum, CN λ 4200 and (Mg I + Mg H) λ 5175, whenever available (BA 87a). Again, objects with a high metallic content exhibit a large spread of their [N II]/Hα and [S II]/Hα line ratios. Finally, we show in Figs. 19a and 19b, the same line ratios against the maximum metallicity attained in the stellar population according to population synthesis models of Bica (1988). *Thus we are testing the gas line ratios directly against the metallicity of the most recent generation of stars in the galaxy nuclei.* For the LMC and SMC we have adopted the average metallicity attained in the H II region sample $[Z/Z_{\odot}] = -0.5$

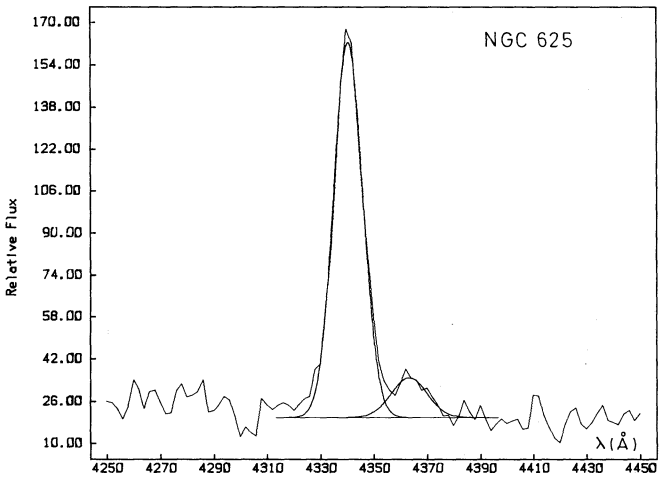

Fig. 8. The gaussian fit in the Hγ,[O III] λ4363 region. Units as in Fig. 1

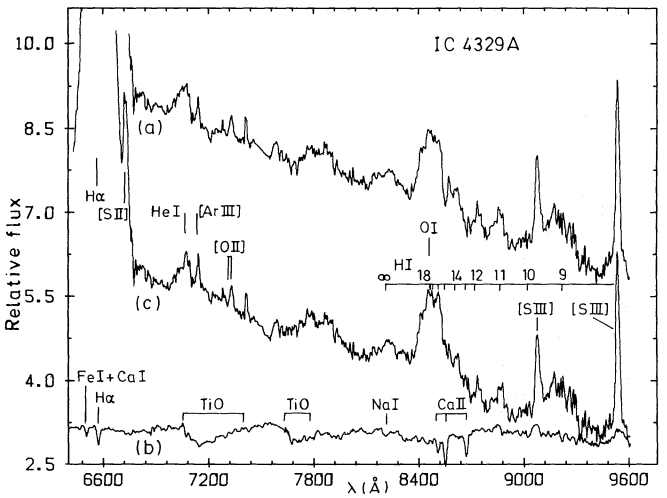

Fig. 9a–c. Illustration of the subtraction procedure in the near-infrared region for the active nucleus in IC 4329 A. **a** Observed spectrum corrected for reddening; **b** template population; **c** subtracted spectrum. See Sect. 4.1 for detail

and $[Z/Z_\odot] = -0.9$ respectively (Bica et al., 1986). It is obvious that the dispersion among metal-rich galaxies persists indicating that another parameter, excitation, plays an important role then. Nevertheless, Fig. 19 also indicates that metallicity is important as well. According to Figs. 17 to 19, the [N II]/Hα line ratio correlates better with metallicity indicators than [S II]/Hα does, suggesting that nitrogen is indeed more closely related to the global metallicity than sulphur.

5.2. Reddening in the line-emitting regions

All reddening sources extrinsic to the line-emitting regions have been taken into account (Sect. 3). It should be noted that none of these corrections is based upon the Hα/Hβ line ratio. They were estimated according to the object's Galactic latitude $|b|$, the stellar population absorption lines and the stellar population continuum distribution (Table 1).

The Hβ gaseous emission component is very often critically entangled with the stellar absorption component. The stellar population subtraction with a proper model template has, however, provided reliable measurements of Hβ in emission (Tables 2 to 5). So we have now 43 objects in our sample with *Hβ and Hα line measurements corresponding to the pure emission component*, as it would appear to an observer located just outside the ionized gas regions. We provide in Fig. 20 an histogram of the observed line ratio Hα/Hβ and the corresponding $E(B-V)$ values assuming the recombination theory *B* case. We have divided our sample into E to Sb (Fig. 20a) and Sc (Fig. 20b) galaxies. The former group contains mostly classical LINERS and the latter mostly H II region nuclei (Heckman, 1980a,b). Both subsamples exhibit a Hα/Hβ peak around the value 4.2, indicating that a typical value of the color excess is $E(B-V) = 0.35$. Some of the values in Fig. 20a fall below the dereddened value 2.86: they correspond to objects with an emission component so weak with respect to the stellar population that the error bar on Hβ is then certainly larger than for the rest of the sample.

As a comparison we show in Figs. 20c and 20d respectively the same quantity for the H II region and for the Seyfert samples. The H II regions are clearly peaked around $H\alpha/H\beta = 4.2$. Considering that the Seyfert subsample is small, its distribution is compatible with the rest of the objects. The complete histogram (Fig. 20) is highly peaked around the value 4.0 and thus we conclude that when all foreground sources of reddening are properly taken into account, the dust to gas ratio within the line-emitting regions of such a wide variety of objects is remarkably uniform.

We cannot perform any detailed line profile study in the case of Seyfert 1 nuclei, owing to the low spectral resolution of our data. However, the gaussian fitting procedure required at least three components for each of the Balmer lines (Hα, Hβ and Hγ). We show in Table 6 the derived Hα/Hβ ratios for each component. At least for the present objects there is a tendency towards smaller Hα/Hβ ratios for the broad component (BLR). Assuming the recombination theory *B* case, this would imply a smaller dust/gas ratio in the BLR than in the NLR. However the high density regime in the BLR is known to significantly lower the Balmer decrement (e.g. Canfield and Puetter, 1981).

5.3. Electron density in the line emitting region

For 65 objects it was possible to deblend the [S II] λλ6717, 31 pair (Tables 2 to 5). Assuming a mean electron temperature $T_e = 10\,000$ K, we can estimate the electron densities for the line emitting region in our sample (McCall, 1984). We show in Fig. 21, the line ratio [S II] λ6717/[S II] λ6731 histograms for different classes of objects and the corresponding electron densities. We show respectively in Fig. 21a galaxies of morphological types from E to Sb; in Fig. 21b, Sc galaxies; and for comparison in Fig. 21c, the amorphous nuclei and normal H II regions; finally in Fig. 21d, Seyfert nuclei. The distributions are peaked around $N_e = 6\,10^2\,\mathrm{cm}^{-3}$. They are in general asymmetric with a steeper slope towards the high density limit (HDL), as the [S II] lines then get collisionally de-excited.

3. Grouping low-level emission galaxy nuclei to access weak lines: a clue to their ionization mechanism

6.1. Rationale of the grouping method

Shock models were early proposed to account for the excitation in LINERS (Koski and Osterbrock, 1976). But later, alternatives

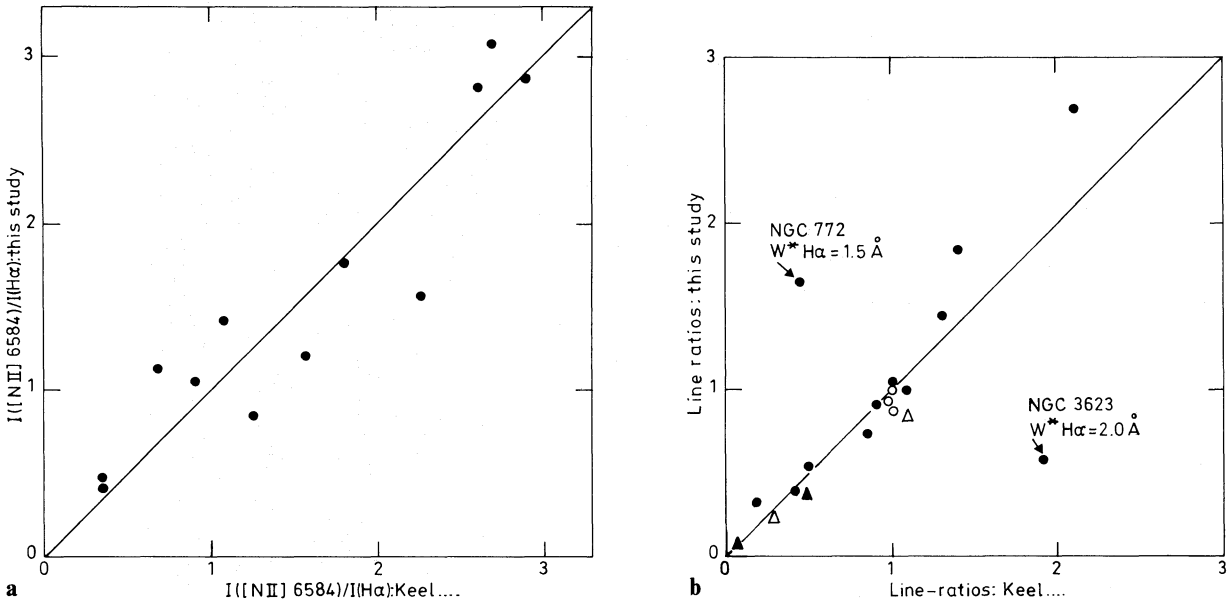

Fig. 10a and b. Comparison of our results with those earlier derived by Keel et al. (1983, 1985). **a** For the [N II] λ6584/Hα line ratio; **b** for various other line ratios: black dots: [S II] $\lambda\lambda$6717, 6731/Hα; open circles: [S II] λ6717/[S II] λ6731; black triangles: [O I] λ6300/Hα; open triangles: [O III] $\lambda\lambda$4959, 5007/Hβ

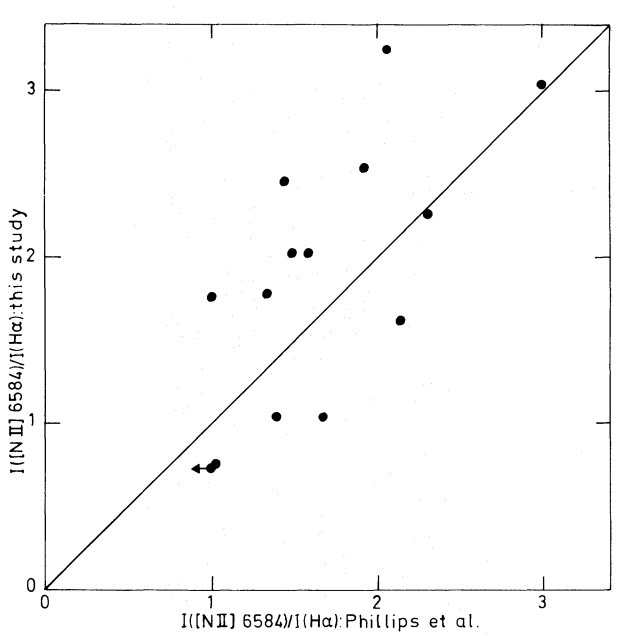

Fig. 11. Comparison of our results to the ones obtained by Phillips et al. (1986), for the line ratio [N II] λ6584/Hα

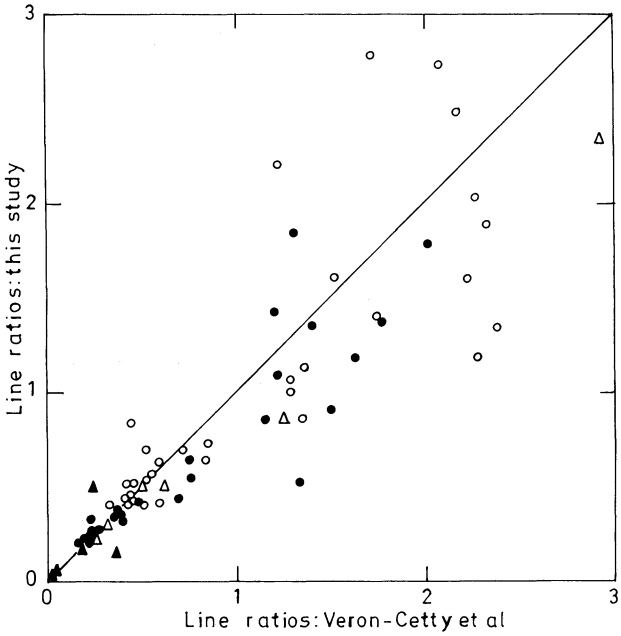

Fig. 12. A confrontation between our measurements and those from Véron-Cetty and Véron (1986) for various line ratios: black dots: [S II] $\lambda\lambda$6717, 6731/Hα; open circles: [N II] λ6584/Hα; black triangles: [O I] λ6300/Hα; open triangles: [O III] λ5007/Hβ

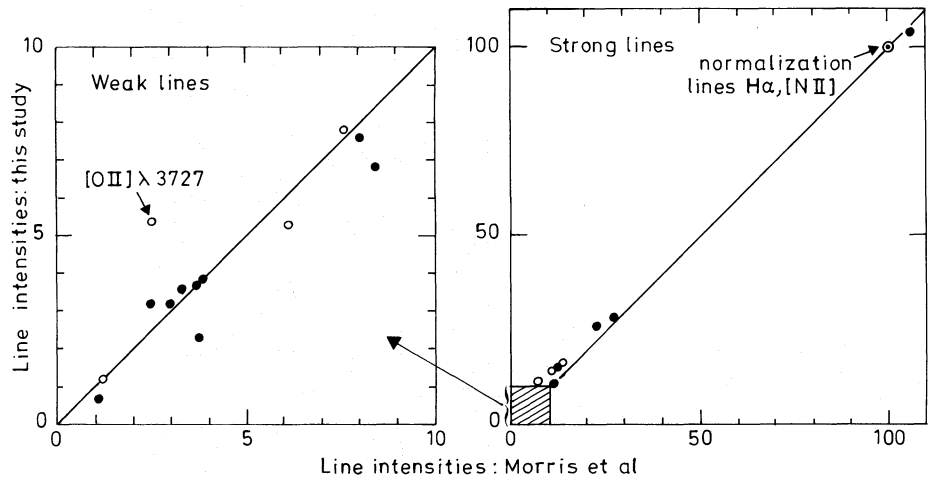

Fig. 13. Comparison of our line measurements to those obtained by Morris and Ward (1988) in 2 galaxies: black dots: NGC 5643; open circles: NGC 6221

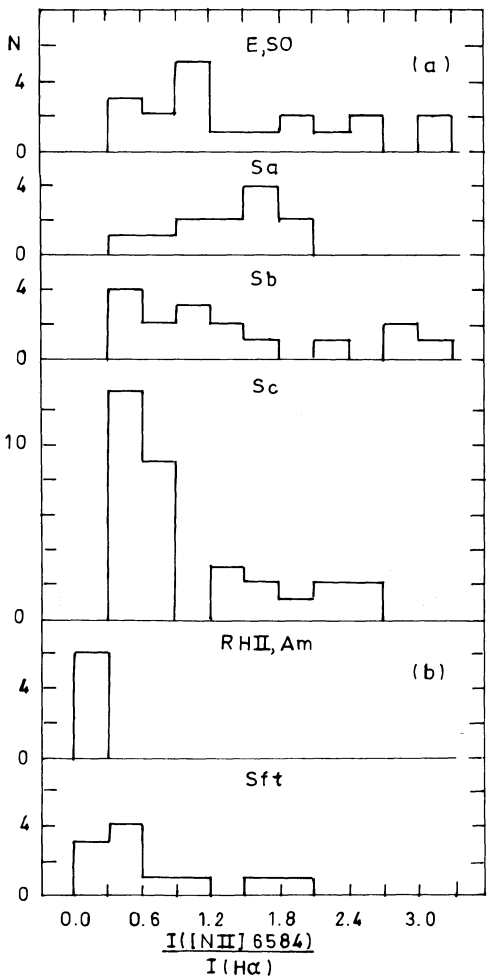

Fig. 14. a Histograms of the [N II] λ 6584/Hα line ratio for galaxies of different morphological types; **b** comparative histograms for H II regions and amorphous galaxies and for Seyfert nuclei

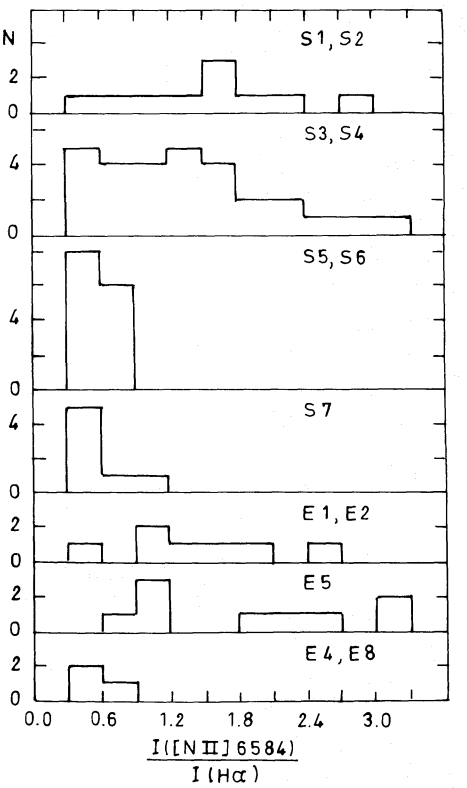

Fig. 15. Histograms of the [N II] λ 6584/Hα line ratio as a function of the underlying spectral type of the nuclear population

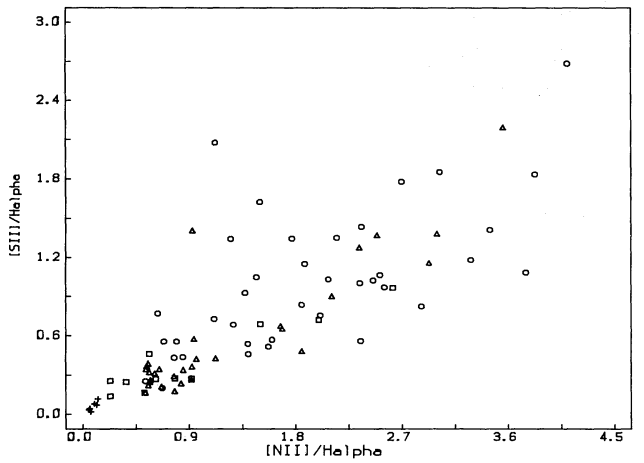

Fig. 16. Correlation between [S II]/Hα and [N II]/Hα line ratios. Circles represent morphological types E to Sb; triangles, Sc galaxies; plus signs, amorphous galaxies and H II regions; squares, Seyfert nuclei

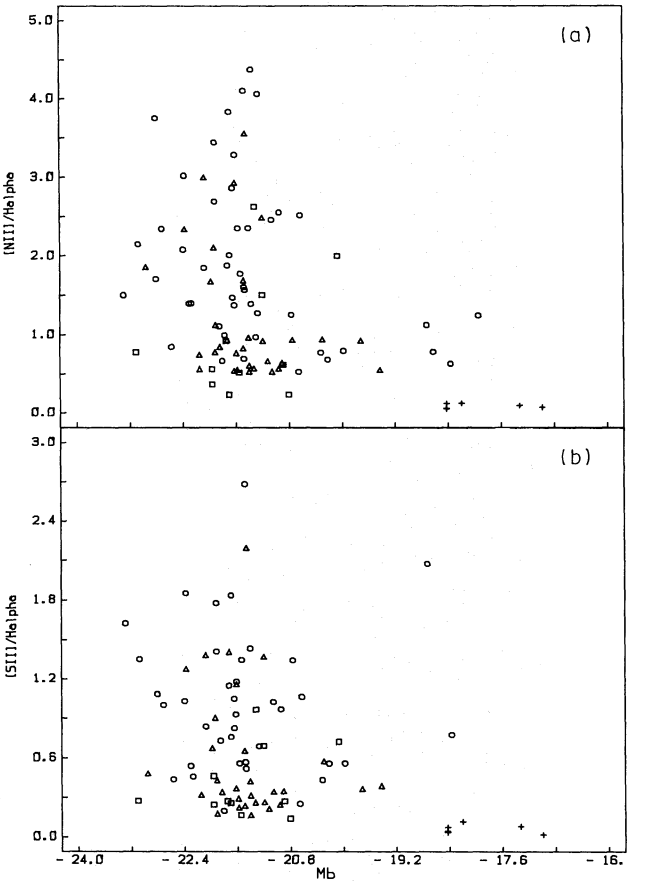

Fig. 17. a The [N II]/Hα line ratio vs. absolute magnitude M_B; **b** same plot for the [S II]/Hα line ratio. Symbols as in Fig. 16

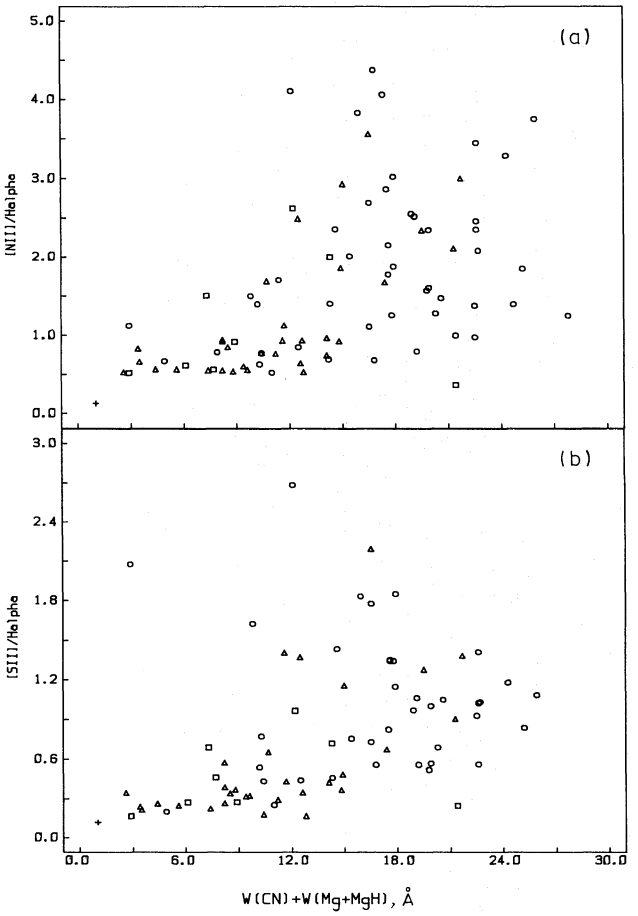

Fig. 18. a The [N II]/Hα line ratio vs. $W(\mathrm{CN}) + W(\mathrm{Mg} + \mathrm{Mg}\,H)$; **b** idem for the [S II]/Hα line ratio. Symbols as in Fig. 16

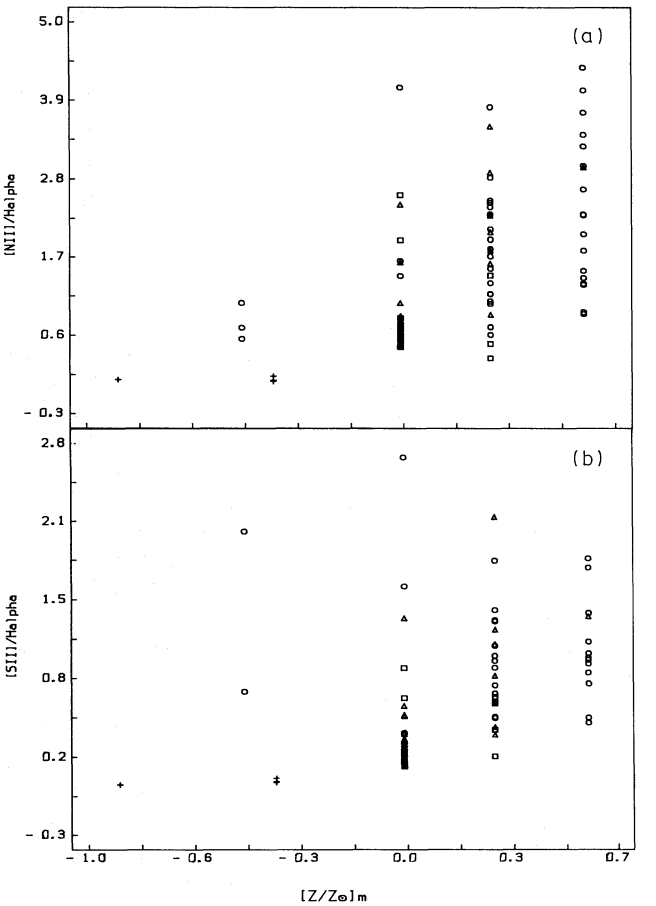

Fig. 19. a The [N II]/Hα line ratio vs. maximum metallicity attained in the stellar population $[Z/Z_{\odot}]_{\mathrm{m}}$; **b** idem for the [S II]Hα line ratio. Symbols as in Fig. 16

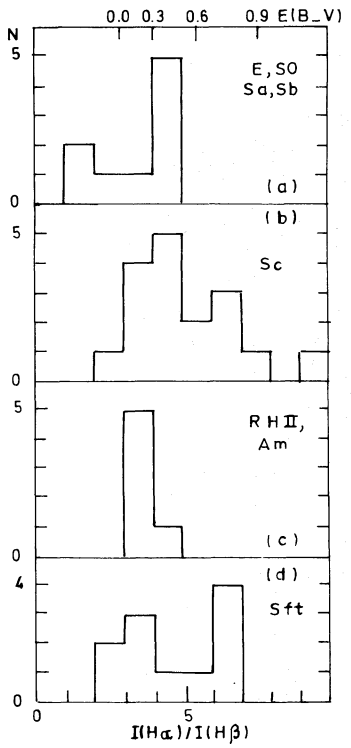

Fig. 20a–d. Histograms of the Hα/Hβ line ratio. Upper scale gives the corresponding color excess

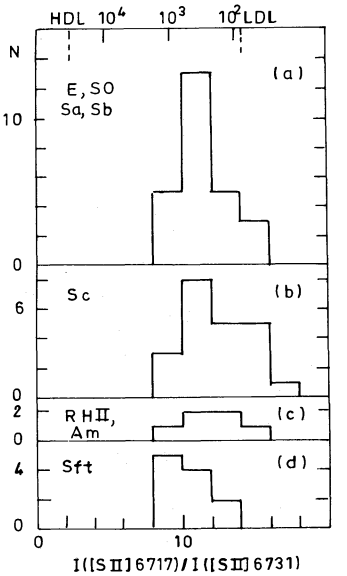

Fig. 21a–d. Histograms of the [S II] λ6717/[S II] λ6731 line ratio. Upper scale displays the corresponding electron density. HDL and LDL mean respectively high and low density limit

Table 6. Balmer decrement for the 3 components in Seyfert 1: narrow (n), intermediate (i) and broad (b)

	(Hα/Hβ)n	(Hα/Hβ)i	(Hα/Hβ)b
NGC 3783	2.9	4.2	1.3
NGC 7469	6.3	5.0	2.5
IC 4329A	6.1	6.2	3.2

were discussed, invoking photoionization by a power-law continuum together with a low ionization parameter (Ferland and Netzer, 1983; Halpern and Steiner, 1983; Keel, 1983; Péquignot, 1984; Binette, 1985), or photoionization by extremely hot stars (Terlevich and Melnick, 1985).

A new clue to this problem recently arose from accessing [S III] λλ 9069, 9532 line measurements. Indeed, shock models with shock velocity around 100 km s^{-1} predict a lower [S III] λλ 9069, 9532/[S II] λλ 6717, 6731 line ratio than do classical photoionization models (DPW). Therefore, this line ratio can be used to discriminate between the two ionization mechanisms. The objects studied in DPW, as well as NGC 1052 (Diaz, Pagel and Terlevich, 1985, hereafter DPT), all are strong LINERS. Their location in the [SII] vs [SIII] diagram favours photoionization as being the main excitation mechanisms in LINERS. In the present study, we push down the detection level at the [SIII] lines by grouping objects in three different classes and hence improving the signal to noise ratio of the spectrum representing each class of objects. It becomes then possible to investigate the ionization mechanism operating in weak LINERS.

6.2. *The groups*

We have restricted our analysis to a subsample of 76 galaxies, out of the initial 92 objects presented in Sect. 2. We have excluded the Seyfert 1 nuclei, 11 galaxy nuclei classified as Seyfert-like in Véron-Cetty and Veron (1987), 2 nuclear HII regions in amorphous galaxies and the metal poor nuclei of NGC 3056, 4476 and 5102 at $M_B > -19$ (Bica, 1988). We are left with 76 objects usually refered to as classical LINERS, nuclear HII regions and extremely low-level emission nuclei with $W^*(\mathrm{H}\alpha) \leq 2$Å. Morphological types of the host galaxies in this subsample vary from spiral to elliptical, their absolute magnitude M_B is in the range $(-19.4, -23.3)$. We emphasize that all galaxies but NGC 692 being from the Shapley-Ames Catalogue, the typical slit used in the observations has average dimensions (0.8 ± 0.5) Kpc × (1.4 ± 0.9) Kpc. Therefore, the average spectrum we build for each group corresponds to the central 1 Kpc size region. Because we aim at measuring the critical [S III] λλ 9069, 9532 lines, we recall that near infrared data were carefully corrected for atmospheric absorptions (BA 87b).

It is clear that our sample of 76 spectra of low-level emission galaxy nuclei spans a wide range in emission-line properties (Sect. 4). However, at least for the strongest lines, Hα, [N II] λλ 6548, 6584 and [S II] λλ 6717,6731, we could see that many objects share similar characteristics. Thus, motivated by the need for obtaining information on weaker lines we decided to group the objects in order to study their average properties.

Similarly to the results from stellar population analysis performed by Bica (1988) where galaxies in boxes of equal morphological type and absolute luminosity do not necessarily exhibit homogeneous spectral absorption properties, we find in the present study that, at a given morphological type and absolute luminosity, quite heterogeneous emission-line spectra can be seen. So, a better approach for generating groups with respect to their line emission properties is to use as a primary criterium for grouping that of similar strong emission-line ratios.

In our sample, all galaxies display measurable Hα and [N II] λλ 6548, 6584 lines, and 88% of them exhibit [S II] λλ 6717, 6731 lines. So we considered the line intensity ratios [N II]/Hα and [S II]/Hα as first order criteria which could be used even in lower signal to noise ratio data. As a result we obtain a first grouping which provides average spectra with improved signal to noise ratio. Other fainter lines such as [O I] λ 6300, Hβ can then be taken into account and this grouping procedure reiterated once more. We ended up with three distinct classes A, B, C, of which galaxy members are listed in Table 7. The use of average spectra enables us to push down the detection level of emission lines and notably to reach $W([\mathrm{S\,III}]\,\lambda 9069) \leq 0.1$ Å. As well, [O III] λλ 4959, 5007 lines have been marginally detected even in the lowest-level emission class C (Fig. 22).

Table 7. Galaxy members of the 3 classes A, B, C, according to the emission level

Group A	NGC 289	NGC 908	NGC 986	NGC 1084	NGC 1637	NGC 2903	NGC 2997
	NGC 3351	NGC 4027	NGC 4038	NGC 4039	NGC 4254	NGC 4303	NGC 4321
	NGC 4535	NGC 4536	NGC 4569	NGC 5236	NGC 5248	IC 5325	NGC 6215
	NGC 6699	NGC 6782	NGC 7392	NGC 7552			
Group B	NGC 692	NGC 1353	IC 1459	NGC 3358	NGC 3623	NGC 3887	NGC 4192
	NGC 4438	NGC 4486	NGC 4501	NGC 4579	NGC 4981	NGC 5064	NGC 5101
	NGC 5156	NGC 5266	NGC 6744	NGC 6868	NGC 7083	NGC 7205	NGC 7410
Group C	NGC 772	NGC 1316	NGC 1371	NGC 1380	NGC 1400	NGC 1553	NGC 2442
	NGC 3054	NGC 3368	NGC 3627	IC 4296	NGC 4374	NGC 4435	NGC 4548
	NGC 4594	NGC 4856	IC 4889	NGC 4936	NGC 4958	NGC 5090	IC 5267
	NGC 5612	NGC 6758	NGC 6776	NGC 6861	NGC 6923	NGC 6925	NGC 6942
	NGC 7049	NGC 7329					

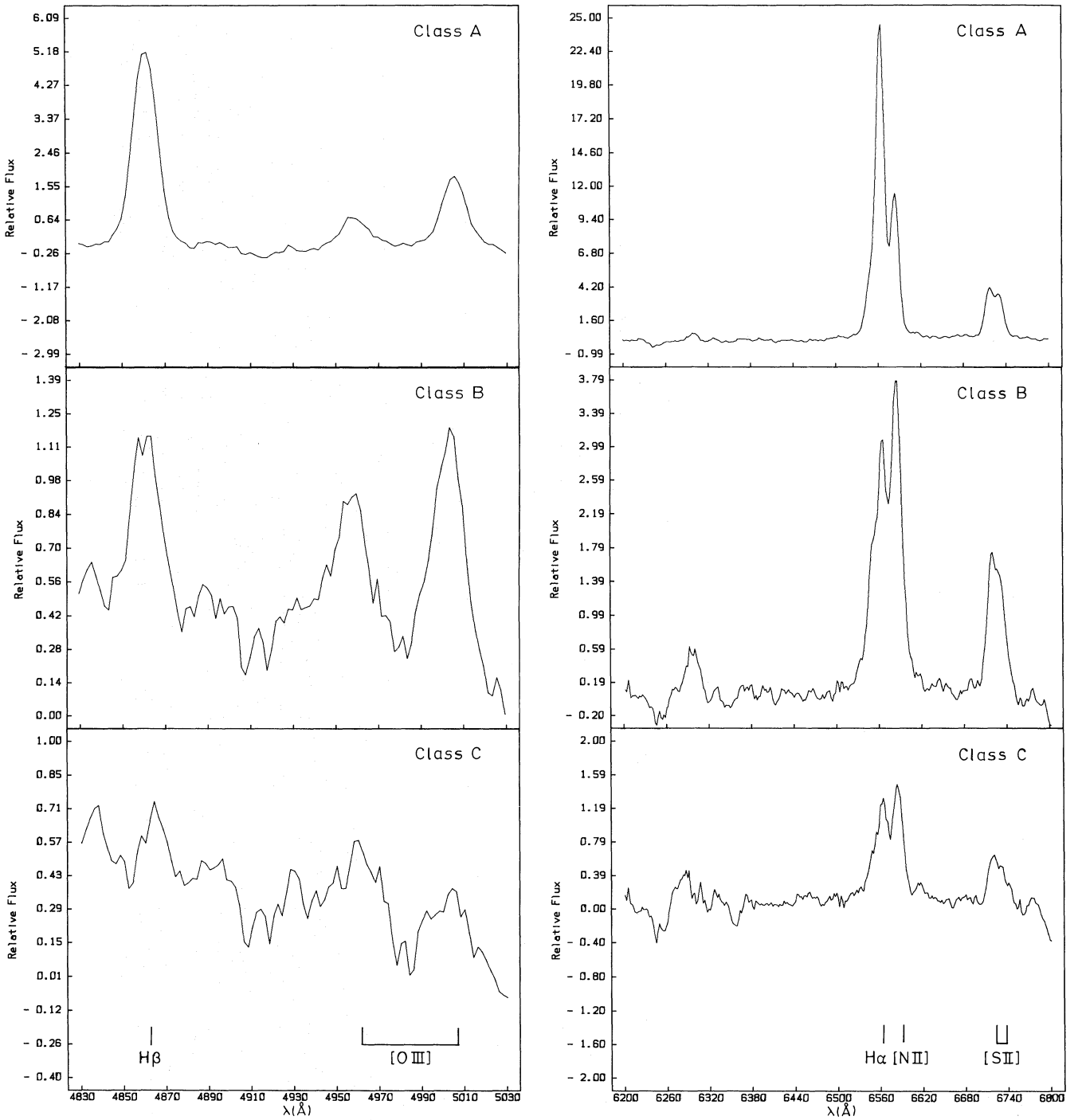

Fig. 22. Galaxy classes A, B and C in order of decreasing emission level. Left panel shows the Hβ, [O III] region: right panel shows the [O I] λ 6300, Hα, [N II], [S II] region. Both regions are from IDS spectra. Flux is in arbitrary unit

6.3. Discussion

For our galaxy classes A, B, and C, in order of decreasing emission level, we present in Fig. 22 the Hβ, [O III] and [O I] λ 6300, Hα, [N II], [SII] regions from IDS spectra, and in Fig. 23, the [S II] and [S III] λ 9532 regions from CCD spectra.

The characteristic emission spectrum of class A objects corresponds to nuclear H II regions as classified by Heckman (1980a). Indeed, in terms of their underlying population all objects of class A belong to the S7, S6 and S5 spectral groups for which a young stellar component is known to be present according to the population synthesis in Bica (1988). The average emission spectrum of class B objects is that of classical LINERS (Heckman, 1980b; Keel, 1983) and indeed strong LINERS like NGC 4579 from Keel's sample are included in our galaxy group B. Objects of class C differ from those of class B in showing a

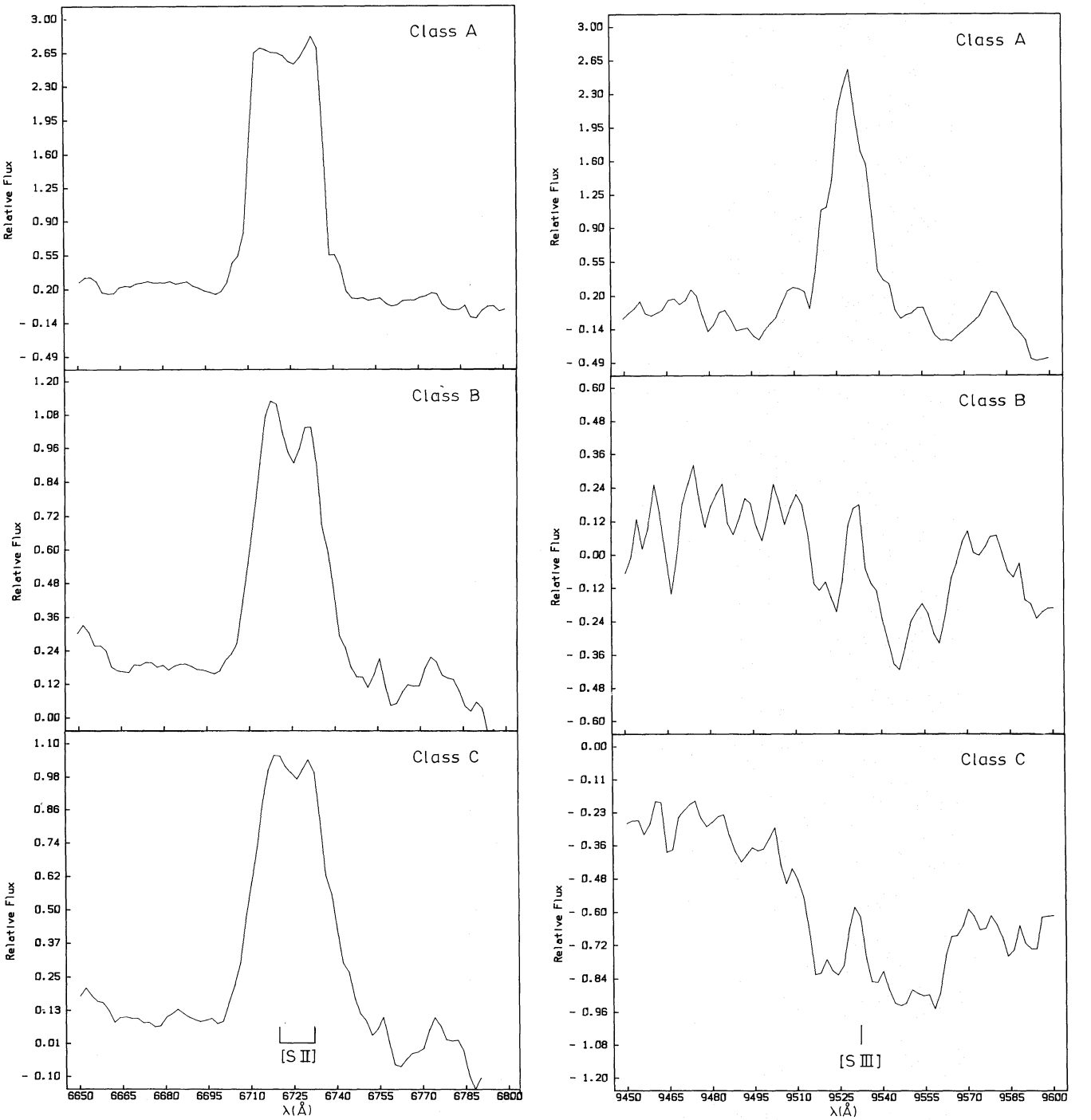

Fig. 23. Galaxy classes A, B and C in order of decreasing emission level. Left panel shows the line pair [S II] λλ 6717, 6731; right panel shows the [S III] λ 9532 line. Both regions are from CCD spectra. Flux is in arbitrary unit

slightly lower excitation and a considerably lower emission level: $W^*(\mathrm{H}\alpha) = 4.6$ Å in group B, while $W^*(\mathrm{H}\alpha) = 1.7$ Å in group C. In groups B and C, the underlying population is largely dominated by a red old component.

For each class we have listed in Table 8 the number of objects in morphological type and absolute magnitude boxes. Group A contains mostly Sb and Sc galaxies, while emission-line nuclei from groups B and C can be found in all morphological galaxy types. Thus we emphasize that Sc galaxies are not necessarily associated with nuclear H II regions but may also host classical LINERS or low-level emission nuclear sources as represented by the average spectrum of class C objects.

We have deblended and measured the intensity of emission lines in our three groups as explained in Sect. 4. Results are given in Table 9, normalized to $I(\mathrm{H}\alpha) = 100$. The upper line for each group lists intensities measured from IDS spectra, and the lower

Table 8. Distribution of galaxy types within each class

Group A	E	S0	Sa	Sb	Sc
$M_B < -22$				2	2
$-22 < M_B < -21$				1	15
$M_B > -21$				1	4
Group B	**E**	**S0**	**Sa**	**Sb**	**Sc**
$M_B < -22$	1		2	1	1
$-22 < M_B < 21$	1	2	3	4	3
$M_B > -21$				1	2
Group C	**E**	**S0**	**Sa**	**Sb**	**Sc**
$M_B < -22$	2		1	2	2
$-22 < M_B < -21$	4	3	3	4	3
$M_B > -21$		3	3		

one lists those obtained from CCD spectra. We also show in Column 2 the pure emission value that $W^*(\mathrm{H}\alpha)$ would have for a continuum height corresponding to the stellar population. Notice that the offset between $W^*(\mathrm{H}\alpha)$ as measured from IDS and CCD spectra is small considering that the galaxies with CCD spectra are a subsample of the IDS set. Also, for both samples the line ratios [N II]/Hα and [S II]/Hα are compatible. In Column 13 we provide the Hα/Hβ line ratio which indicates that another faint source of reddening, intrinsic to the line-emitting region, must be taken into account. Assuming case B recombination theory for the Balmer decrement, we have calculated the corresponding color excess $E(B-V)$ which is given in the last column of Table 9. Table 10 lists dereddened intensities normalized to $I(\mathrm{H}\alpha) = 100$. We recall that the individual spectra used to build up the average spectrum for each class of objects had been previously corrected for sources of reddening *external* to the line emitting regions, according to the procedure described in Sect. 3. The reddening *internal* to the line-emitting regions in objects of classes A, B and C makes the Hα/Hβ line ratio be around 4 (Table 10), similar to that observed in individual strong-lined galaxy nuclei (Sect. 5.2). Thus, we find evidence that, on average, weak-lined and strong-lined galaxy nuclei have a similar dust content–in terms of gas/dust ratio–.

Following DPW we have plotted in Fig. 24 the line ratios [S II]/Hα vs. [S III]/Hα, and in Fig. 25 [S II]/[SIII] vs. [O II]/[O III] for the characteristic spectra in groups A, B and C. We have indicated with an arrow, the effect of internal reddening. We have also displayed whenever possible, values corresponding to H II regions, to Seyfert-like, Seyfert 2 and the narrow line region of Seyfert 1 nuclei. Notice that these points are in fair agreement with the loci of similar objects in DPT's analysis. As expected, the characteristic spectrum for class A objects tends to look like that of normal H II regions, although it is less excited. This lower excitation, as denoted by a lower [O III]/Hβ line ratio is not necessarily due to higher metallicity. Indeed H II regions in nuclei are spatially very crowded (Sersic and Pastoriza, 1965). The question of H II region evolution has been discussed by Copetti et al. (1986). This lower [O III]/Hβ line ratio may

Table 9. Emission line measurements for each class of objects, A, B, and C

		$W^*(\mathrm{H}\alpha)$	[O II] 3727	Hβ	[O III] 5007	[O I] 6300	Hα	[N II] 6584	[S II] 6717	[S II] 6731	[S III] 9069	[S III] 9532	Hα/Hβ	$E(B-V)$
A	IDS	34.4	19.1	23.2	9.1	3.1	100	48.6	15.0	13.3			4.3	0.38
	CCD	28.9					100	53.5	12.6	13.0	5.6	13.1		
B	IDS	4.6	71.2	25.8	43.5	33.1	100	149.9	57.9	42.5			3.9	0.28
	CCD	4.0					100	94.6	32.9	29.2	3.0	12.1		
C	IDS	1.7	⩽150.1	19.8	34.4	63.7	100	136.3	49.0	35.1			5.1	0.53
	CCD	2.3					100	168.1	68.8	65.6	3.6	7.3		

Table 10. Relative line intensities corrected for intrinsic reddening, in the mean spectra corresponding to objects classes A, B and C

		[O II] 3727	Hβ	[O III] 5007	[O I] 6300	Hα	[N II] 6584	[S II] 6717	[S II] 6731	[S III] 9069	[S III] 9532
A	IDS	39.9	34.9	13.1	3.2	100	48.5	14.6	12.8		
	CCD					100	53.3	12.3	12.6	4.0	9.0
B	IDS	122.4	34.8	57.0	34.4	100	149.5	56.7	41.6		
	CCD					100	94.3	32.3	28.5	2.3	9.2
C	IDS	⩽419.5	35.0	57.4	68.6	100	135.6	47.2	33.6		
	CCD					100	167.3	66.1	62.7	2.2	4.3

simply reflect an accumulation of H II regions at different evolutionary stages, dominated by old, less excited H II regions. The fact that a considerable fraction of the underlying stellar population ranges at ages from 10^7 to $3\,10^8$ yr, particularly in group S7 (Bica, 1988), indicates that star formation has been occurring over a long period and suggests that components in the stellar population have ages distributed between $5\,10^6$ to 10^7 yr, corresponding to the late stages of an H II region evolution.

The characteristic spectrum for class C objects is unambiguously located in both diagrams in the shock-excited region with shock velocity in the range 100–200 km s^{-1}. The reddening arrows show that this conclusion would not be affected by internal reddening. We would like to stress that *this result could be obtained only because we have considerably lowered the detection level of faint emission lines by grouping objects and averaging spectra selected on the basis of their strong emission line characteristics.* We have interpreted the relative emission peak at λ9532 (Fig. 23) in the average spectra corresponding to groups B and C as a positive detection of the [S III] λ9532 line. The water vapour high spatial frequency residuals tend to cancel out in the average spectrum owing to the different redshifts of the galaxies. Lower spatial frequency residuals, however tend to remain, like the depression where this line is located. We think this does not affect seriously the [S III] λ9532 line measurement, as long as a local continuum is used: we have also measured the [S III] λ9068 line and find indeed a consistent line intensity ratio (Tables 9 and 10).

The characteristic spectrum for class B objects sits at an intermediate position between shock-excited and photoionization model, nearer to the former, however LINERS in DPW's sample fall closer to photoionization models, as NGC 1052 which we have also plotted in Figs. 24 and 25 using DPT's data. The sequence from C to B and to DPW's objects plus NGC 1052 is a sequence of increasing intensity of the emission component relative to the stellar population. The diagrams also show that the emission line characteristics on average vary along this sequence.

We also used the diagnostic diagrams described in Baldwin, Phillips and Terlevich (1981, hereafter BTP) in order to check the consistency of our results. In Fig. 26 we have plotted the line ratios [N II] λ6584/Hα vs. [O II] λ3727/[O III] λ5007 and as expected the average class A object falls in the area of H II regions whereas class B and class C (upper limit in [O II] λ3727) objects are in the shock-excited region. The same conclusion can be derived from Fig. 27 in which we have displayed the $<E>$ index as defined in BPT against the line ratio [O II] λ3727/[O III] λ5007. It would be important to measure more precisely the [O II] λ3727 line intensity for objects of class C, in order to refine the diagnostic. The latter two diagnostic diagrams are used only as a consistency check because recent photoionization models by Ferland and Netzer (1983) now span the "shock-excited" locus in Fig. 26 only by varying the chemical abundance and

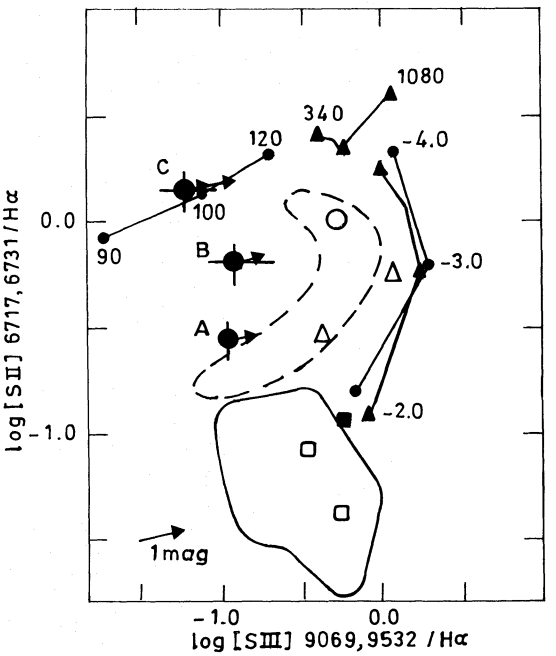

Fig. 24. Logarithmic plots of line intensity ratios [S II]/Hα versus [S III]/Hα. Theoretical models as in DPW: labels 90 to 1080 represent velocities in km s^{-1} of the shock-wave model: -2.00 to -4.00 represent log(U) for photoionization models: black dots labelled A, B and C refer to our line-emission classes: an open circle represents NGC 1052 according to DPT: the area delineated by a continuous line contains H II regions (DPW): that delineated by the dashed line DPW's LINERS and NLR in Seyfert 1 galaxies; open squares are H II regions from our sample; the filled square corresponds to the H II region nucleus in the amorphous galaxy NGC 5323; open triangles stand for Seyfert-like galaxies from our sample

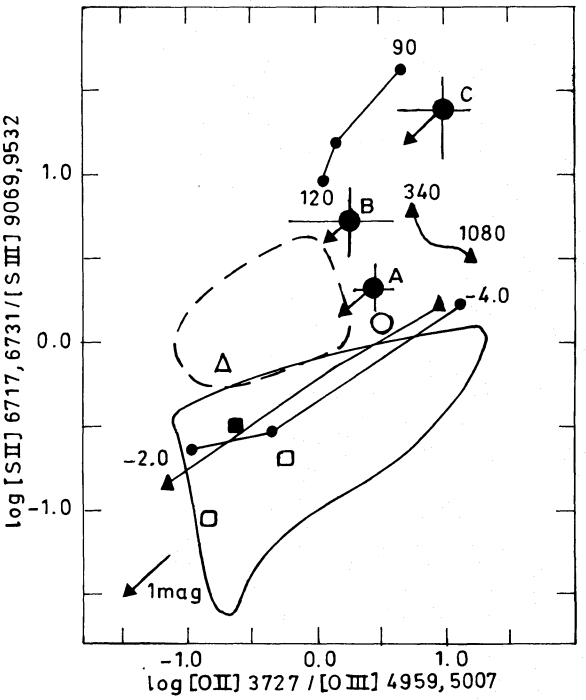

Fig. 25. Same as Fig. 24 but for the line-ratios [S II]/[S III] vs. [O II]/[O III]

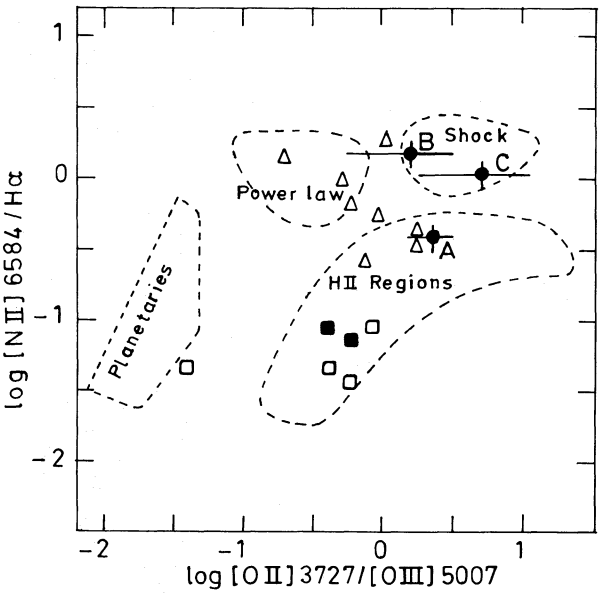

Fig. 26. Logarithmic plots of the line intensity ratios [N II] λ6584/Hα versus [O II] $\lambda\lambda$3727, 29/[O III] λ5007. We have indicated the regions containing most of BPT's objects. Symbols as in Fig. 24

ionization parameter. But we would like to stress the fact that models by Ferland and Netzer (1983) or diagrams in BPT use line-ratios in the visible region only: these line-ratios are not sensitive discriminators of the excitation mechanism, in contrary to [S III] $\lambda\lambda$9069, 9532 and [S II] $\lambda\lambda$6717, 6731 (DPW, DPT). As far as we are aware, no attempt has been made, from a theoretical point of view, to test whether the shock-excited locus involving [S III] lines in Figs. 24and 25 can be spanned by some combination of parameters in photoionization models; it would be important to test this possibility.

7. Concluding remarks

We have analyzed the emission-line properties of a sample of 92 galaxies after having subtracted appropriate absorption templates and corrected the spectra for all sources of reddening extrinsic to the line-emitting regions. Our galaxy sample being from the Shapley-Ames Catalogue, the observations correspond, on average, to the central Kpc^2. We find that the [N II] $\lambda\lambda$6548,84 lines are slightly more sensitive to metallicity effects than are the [S II] $\lambda\lambda$6717, 31 lines. However, both lines are very sensitive to excitation as well. The distribution of the Hα/Hβ line ratio as found in the pure line-emitting regions is peaked around the same value 4.2 suggesting a similar dust to gas content in these regions for classes of objects as different as H II regions, classical LINERS, Seyfert 2 and NLR of Seyfert 1 nuclei. The distribution of the electron density in the line emitting regions of our sample galaxies is sharply peaked around $N_e = 610^2\,\mathrm{cm}^{-3}$.

In order to push down the detection level for measuring critical weak emission lines, we have built from a subsample of 76 low-level emission galaxy nuclei, the average spectra corresponding to three classes of objects selected through their strong emission line characteristics. Class A objects correspond to nuclear H II regions, class B objects represent classical LINERS within an intrinsic luminosity range and class C objects are extremely low-level emission galaxy nuclei. We have been able to measure emission lines to an unprecedent weak level, in particular the [S III] $\lambda\lambda$9069, 9532 lines. These results allow to set constraints on the ionization mechanism at work in each class of objects. In particular, we find evidence that in extreme low-level emission objects of class C, with $W^*(\mathrm{H}\alpha) \leq 2$ Å, the *emission line spectrum arises from shock-ionized gas.* For higher level emission objects of classes B and A, photoionization sources become progressively dominant.

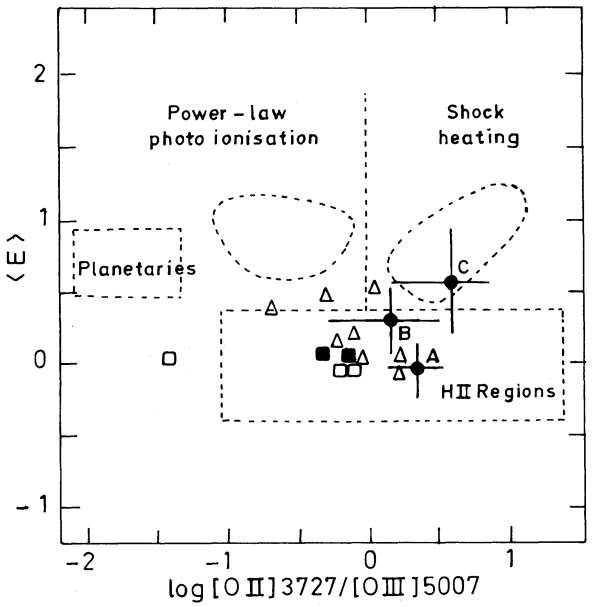

Fig. 27. The index $\langle E \rangle$ as defined in BPT vs. log([O III] $\lambda\lambda$3727, 29/[O III] λ5007). Regions and symbols as in Fig. 26

Acknowledgements. E.B. and C.B. acknowledge the brazilian Institution CNPq for fellowship. In addition, E.B. thanks the Observatoire de Paris for financial support through a temporary assistant position. We are finally indebted to B. Pagel for interesting comments on an earlier version of this work.

References

Baldwin, J.A., Phillips, M.M., Terlevich, R.; 1981, *Publ. Astron. Soc. Pac.* **93**, 5
Bica, E., Alloin D.: 1986a, *Astron. Astrophys.* **162**, 21
Bica, E., Alloin D.: 1986b, *Astron. Astrophys.* **166**, 83
Bica, E., Alloin D.: 1987a, *Astron. Astrophys. Suppl. Ser.* **70**, 281
Bica, E., Alloin D.: 1987b, *Astron. Astrophys.* **186**, 49
Bica, E., Dottori, H., Pastoriza, M.: 1986, *Astron. Astrophys.* **156**, 261
Bica, E.: 1988, *Astron. Astrophys.* **195**, 76
Binette, L.: 1985, *Astron. Astrophys.* **143**, 334
Canfield, R. Puetter, R.: 1981, *Astrophys. J.* **243**, 390
Copetti, M., Pastoriza, M., Dottori, H.: 1986, *Astron. Astrophys.* **156**, 111
Diaz, A., Pagel, B., Wilson, R.: 1985, *Monthly Notices Roy. Astron. Soc.* **212**, 737
Diaz, A., Pagel, B., Terlevich, E.: 1985, *Monthly Notices Roy Astron. Soc.* **214**, 41P
Dufour, R., Harlow, W.: 1977, *Publ. Astron. Soc. Pac.* **89**, 630
Ferland, G., Netzer, H.: 1983, *Astrophys. J.* **264**, 105
Halpern, J., Filippenko, A.: 1984, *Astrophys. J.* **285**, 475
Halpern, J., Steiner, J.: 1983, *Astrophys. J.* **269**, 237
Heckman, T.: 1980a, *Astron. Astrophys.* **87**, 142
Heckman, T.: 1980b, *Astron. Astrophys.* **87**, 152
Keel, W.: 1983, *Astrophys. J.* **269**, 466
Keel, W., Kennicutt, R., Hummel, E., van der Hulst, J.: 1985, *Astron. J.* **90**, 5
Koski, A., Osterbrock, D.: 1976, *Astrophys. J.* **203**, 249
Martin, W.: 1974, *Monthly Notices Roy. Astron. Soc.* **168**, 109
Mathis, J., Chu, Y.H., Peterson, D.: 1985, *Astrophys. J.* **292**, 155
McCall, M.: 1984, *Monthly Notices Roy. Astron. Soc.* **208**, 253
Morris, S., Ward, M.: 1988, *Monthly Notices Roy. Astron. Soc.* **230**, 639
Pagel, B.: 1983, in *Formation and Evolution of Galaxies and Large Structures in the Universe*, eds. J. Audouze, J.T. Van, Reidel, Dordrecht, p. 437
Pastoriza, M.: 1979, *Astrophys, J.* **234**, 837
Péquignot, D.: 1984, *Astron. Astrophys.* **131**, 159
Phillips, M., Charles, P., Baldwin, J.: 1983, *Astrophys.* **266**, 485
Phillips, M., Jenkins, C., Dopita, M., Sadler, E., Binette, L.: 1986, *Astron. J.* **91**, 1062
Sersic, J., Pastoriza, M.: 1965, *Publ. Astron. Soc. Pac.* **77**, 287
Stauffer, J.: 1982a, *Astrophys. J.* **262**, 66
Stauffer, J.: 1982b, *Astrophys. J. Suppl. Ser.* **50**, 517
Terlevich, R., Melnick, J.: 1985, *Monthly Notices Roy. Astron. Soc.* **213**, 841
Testor, G., Pakull, M.: 1985, *Astron. Astrophys.* **145**, 170
Véron-Cetty, M.P., Véron, P.: 1986, *Astron. Astrophys. Suppl. Ser.* **66**, 335
Véron-Cetty, M.P., Véron, P.: 1987, *ESO Scientific Report*, No. **5**
Welch. G.: 1970, *Astrophys. J.* **161**, 821
Wilson, A., Penston, M.: 1979, *Astrophys. J.* **232**, 389